OPTICAL STUDIES ON THE PHOTOPHYSICAL PROPERTIES OF STRONGLY QUANTUM CONFINED LEAD BROMIDE PEROVSKITE NANOCRYSTALS

A Dissertation

by

XUETING TANG

Submitted to the Graduate and Professional School of
Texas A&M University
in partial fulfillment of the requirements for the degree of

DOCTOR OF PHILOSOPHY

Chair of Committee,	Dong Son
Committee Members,	Sarbajit Banerjee
	Matthew Sheldon
	Pao Tai Lin
Head of Department,	Simon North

May 2023

Major Subject: Chemistry

ABSTRACT

Recently, lead halide perovskite (LHP) materials have drawn great research interest in the fields of photonics and photovoltaics as sources of photon and charge carriers thanks to their high defect tolerance and carrier mobility. In contrast to traditional semiconductor materials where the band gap is mostly tuned through size, LHP materials showed tunability in the band gap through continuously variable halide components, which eases the synthesis and device fabrication processes. However, recent advances in the synthetic methods of strongly quantum confined LHP nanocrystals (NCs) have largely expanded the research potential of these materials.

In addition to altering the band gap, imposing strong quantum confinement to LHP materials also modifies their electronic properties as a result of increased interaction of the electron and hole pair and excitons with other degree of freedom due to increased spatial overlap. For instance, strong quantum confinement is known to modify the fine structures of exciton states as a result of increased exchange energy of electron and hole, inverting the relative ordering of the bright and dark exciton states of LHP NCs as compared to their weakly quantum confined counterparts.

In hybrid LHP NCs, the presence of an organic A-site cation, usually methylammonium (MA^+) or formamidinium (FA^+), introduces in additional degrees of freedom from the rotational and librational motions of the organic cations. In order to explore the role of the organic cations on the exciton transitions, the photoluminescence (PL) spectra and dynamics of strongly quantum confined $FAPbBr_3$ NCs were investigated.

These $FAPbBr_3$ NCs showed intense emission from the dark exciton ground state, with significantly shorter dark exciton lifetime in comparison to $CsPbBr_3$ NCs of the same size, suggesting the stronger mixing of bright and dark state.

Moreover, the inter-particle electronic coupling in the arrays of strongly quantum confined $CsPbBr_3$ NCs were investigated by means of PL spectra and dynamics as well. The electronic coupling alters the level structure and relaxation dynamics of bright and dark exciton. The results of electronically coupled $CsPbBr_3$ NCs resembles individual NCs of increased sizes, suggesting delocalization of exciton wavefunction beyond borders of NCs in the electronically coupled arrays.

ACKNOWLEDGEMENTS

First of all, I would like to thank my advisor, Dr. Son. He has taught me so much during these years, about science, about how to conduct scientific experiments, and about how to think like a scientist. Being a great scientist himself, he has all the knowledge and experiences in our field of research. And during the years, he passed that knowledge to me gradually by guiding me and inspiring me with the correct way of learning instead of pouring the concepts to me. With his help, I gained not only the knowledge itself, but also the ability to learn things on my own. Growing up being a quick learner of concepts, I had developed the bad habit of jumping to conclusions without thinking deeply beneath the phenomena without even realizing it. Dr. Son, made so much effort stopping me from continuing down the routes. I am so grateful to have him as my advisor to teach me the rights and corrects my wrongs.

I am also very grateful to the senior group members, Dr. Yitong Dong, Dr. Daniel Rossi, Dr. Hsu-Cheng Cheng and Dr. Tian Qiao. They did not only help me with specific operational details the experiments, but also helped me learn how to design experiments efficiently. Their exceptional performance in research also inspired me towards becoming a good scientist as well. Moreover, I am also glad to work with my other fellow group members, Joe, Eric and Connor. For a lot of times, they helped me look at my research projects more clearly with their perspectives. Overall, I feel really delightful working with all of my group members in a loving and helping environment. It has made my graduate study so much easier.

I would also like to thank my collaborators from the Department of Physics, Dr. Xiaohan Liu, Mohit Khurana and Lanyin Luo. They have helped so much on the low temperature spectroscopic experiments, both in terms of carrying out the experiments and explaining to me about the design and alignments of the optical setups. I am especially grateful for Mohit and Lanyin, who sacrificed a lot of their personal time to help me with my experiments when I needed the data in a hurry. Only with their help and supports, I was able to finish those projects nicely and completely. In addition, I would also like to pay my special tribute to Dr. Alexey Akimov, who put a lot of efforts to answer my questions about the physical pictures and optical setups even remotely in Russia.

Personally, I am also really grateful to my parents, my grandma and all of the great friends I have made here in Texas A&M. Life in the graduate school has always been very challenging, but upon that, the difficulties add up when we also experienced the covid shut-down and winter storm. I cannot imagine going through all of these without your company. When I look back on my graduate school days, I always think of the time when you guys telling me it's going to be okay, on the days I complained about how difficult the experiments are, and on the nights I cried about not being able to meet my advisor's standards. You guys have truly been my support through these years.

At last, I would like to thank myself for not giving up. In the end, all the hard work pays back. So, keep fighting, as life goes on.

CONTRIBUTORS AND FUNDING SOURCES

Contributors

This work was supervised by a dissertation committee consisting of Professor Dong Hee Son, Professor Matthew Sheldon, Professor Sarbajit Banerjee of the Department of Chemistry and Professor Pao-tai Lin of the Department of Electrical and Computer Engineering.

The data acquisition of magnetic field dependent exciton dynamics was made by Mohit Khurana and Lanyin Luo from the Department of Physics. The streak camera measurements were performed by Dr. Daniel Rossi from IBS.

All other work conducted for the dissertation was completed by the student independently.

Funding Sources

This work was made possible in part by National Science Foundation under Grant Number CHE-2003961 and Texas A&M University under the X-grants. Its contents are solely the responsibility of the authors and do not necessarily represent the official views of the National Science Foundation and Texas A&M University.

NOMENCLATURE

2D	2-Dimensional
3D	3-Dimensional
CM	Confocal Microscopy
DDAX	Didodecyldimethylammonium Halide
DMF	Dimethylformamide
FA	Formamidinium
LARP	Ligand-Assisted Reprecipitation
LED	Light Emitting Device
LHP	Lead Halide Perovskite
LO	Longitudinal Optical
MA	Methylammonium
MHP	Metal Halide Perovskite
NC	Nanocrystal
NPL	Nanoplatelet
NW	Nanowire
OA	Oleic Acid
ODE	1-Octadecene
OLA	Oleylamine
OLAB	Oleylammonium Bromide
OLAX	Oleylammonium Halide

PEAB	Phenylethyl Ammonium Bromide
PL	Photoluminescence
PLQY	Photoluminescence Quantum Yield
PS	Polystyrene
QD	Quantum Dots
SEM	Scanning Electron Microscopy
SL	Superlattice
TEM	Transmission Electron Microscopy

TABLE OF CONTENTS

Page

LIST OF FIGURES

Page

LIST OF TABLES

Page

1. CHAPTER I

INTRODUCTION

Since the first report of the exceptional performance that LHP materials have as absorbers in dye sensitized solar cells[1-3], explorations on these materials have been extensively carried through. Up till now, the record power conversion efficiency of all perovskite solar cell has reached 24.4%[4], approaching the record power conversion efficiency reported for traditional silicon solar cells. Their exceptional performance in photovoltaics was attributed to their high absorption cross section, high charge carrier mobility and long charge carrier lifetime.

More studies on the photophysical of LHP materials revealed near unity PL quantum yield (PLQY) without any surface passivation, which was attributed to their high defect tolerance from their electronic structure, making them promising candidates as light source materials. Thus, research interest on the LHP materials has soon been broadened into the fields of light emitting devices (LEDs) and semiconductor lasers[5, 6], where their performance has also stood out in comparison to traditional semiconductor materials. Another reason for the prosperity of LHP materials as light source materials also lies on the highly tunable band gap solely through the alternation of the composition, in contrast to traditional semiconductor materials, whose band gap turnability depends on the degree of quantum confinement. With alternation of the ratio of the halide composition, the emission color can be tuned smoothly throughout the entire visible spectral range.

However, even though the utilization of mixed halide LHP materials in LEDs greatly eases the fabrication process, the resulting devices suffer from ion migration under electric field or light illumination[7]. The ion migration leads to phase segregation and emission instability that impairs their applications. Recently, research focus has been transited onto utilization of quantum confinement in LHP NCs to compensate for the photo instability of mixed halide LHP materials in LEDs. Interestingly, LHP NCs in the strongly quantum confined regime, or LHP quantum dots (QDs), have not only exhibited size dependent band gap, but also other properties, such as exciton fine structure splitting, exciton phonon coupling, multiexciton relaxation dynamics, *etc*.

In LHP QDs with lateral sizes smaller than the exciton Bohr diameter, the excitons are spatially confined within the volume of the QDs. The spatial confinement of the excitons results in stronger interaction of the electron and the hole. Previous studies on $CsPbBr_3$ QDs have observed bright and dark exciton level reversal and increased bright dark exciton splitting energy as the size of the QDs decreases, as a result of increased electron and hole exchange energy in smaller QDs[8]. The stronger overlap also increases the coupling between excitons and other degree of freedom, making their photophysical properties more susceptible to the compositional or environmental changes that introduces in other degrees of freedom. For instance, previous studies on the temperature dependent PL in the $CsPbBr_3$ QDs have revealed stronger coupling to phonon modes with smaller sizes[9]. Here in this dissertation, we studied the photophysical properties of these strongly quantum confined LHP NCs and their coupling with other degrees of freedom in detail with spectroscopic methods.

Firstly, for the purpose of studying the influence of an organic A-site cation on the exciton transitions in strongly quantum confined LHP NCs, we investigated the PL properties of $FAPbBr_3$ QDs and compared the results to those of $CsPbBr_3$ QDs. For this purpose, we first developed the synthetic protocol for $FAPbBr_3$ QDs in the strongly quantum confinement size regime. With these materials, the PL spectra and dynamics were first investigated at room temperature, where the information of the size dependent band gap and exciton relaxation can be extracted. Following that, the investigation was extended down to liquid helium temperature. The temperature dependent PL spectra gave the information on the exciton phonon coupling, while the PL dynamics at cryogenic temperature gave the information of the exciton fine structure. The effects of the organic cation in $FAPbBr_3$ QDs were found to have impacts on both the exciton phonon coupling and mixing of the bright and dark exciton state.

In addition to investigation of exciton coupling with intra-QD degree freedom, we are also interested in investigation on the inter-QD electronic coupling in the arrays of strongly quantum confined $CsPbBr_3$ NCs. In semiconductor QDs, the electronic states in individual QDs can be described with the particle in a box model. Inter-QD electronic coupling escribed the case where multiple QDs are brought close enough to each other, the electron wavefunction of QDs overlaps and works as perturbation to the original solution. Inter-QD electronic coupling alters not only the band gap energy of the QD ensemble, but also the exciton fine structure of the QDs in the electronically coupled QD ensemble. For the investigation of the influence of electronic coupling on the exciton fine structure, we studied both the level structure and relaxation dynamics of bright and dark

exciton at cryogenic structure. And the experimental results revealed electronically coupled $CsPbBr_3$ NCs resembles individual NCs of increased effective QD sizes in the presence of electronical coupling.

This dissertation is organized as follows. Chapter II introduces the research background of the synthesis and photophysical properties of LHP NCs. Chapter III includes the introduction of the synthetic methods for strongly quantum confined $FAPbBr_3$ QDs, followed by discussion on the influence of an organic A site cation on the photophysical properties of strongly quantum confined LHP NCs. Chapter IV discusses the preparation of closely-packed 2D arrays of strongly quantum confined $CsPbBr_3$ QDs, which allows for exploration of the influence of electronic coupling on the behavior of bright and dark excitons in the QDs. Lastly, Chapter V summarizes the results and discusses the proposal of future plans for the strongly quantum confined LHP NCs research, including utilization of 3D superlattices made from electronically coupled strongly quantum confined $CsPbBr_3$ QDs for super radiant emission.

2. CHAPTER II

BACKGROUND AND LITERATURE OVERVIEW

2.1. Synthesis and Post-synthetic Surface Treatments of Lead Halide Perovskite Nanocrystals

Perovskite materials stand for a class of crystal structure of ABX_3 stoichiometry. They usually form crystals with cubic lattices, with the A-site cation occupying all the corners, the B-site cation occupying all the body-center position and the X anion occupies all the face-center position. In LHP, the B-site cation is lead (Pb^{2+}), X anions can be chorine (Cl^-), bromine (Br^-), iodine (I^-) or the mixture of them. The A-site cation can be either inorganic, such as cesium (Cs^+) or rubidium (Rb^+), or organic, such as methylammonium (MA^+) or formamidinium (FA^+).

In contrast to traditional semiconductor materials that are mostly covalently bonded, the chemical bonds in LHP materials are highly ionic. As a result, this type of materials is characterized for their structural lability and compositional flexibility, making it relatively easy for colloidal synthesis and solution phase post-synthetic treatment including cation/anion exchange and ligand exchange. In this part of the dissertation, the advances of synthetic methods and ligand exchanges will be discussed.

2.1.1. Synthesis of Lead Halide Perovskite Nanocrystals

For the synthesis of LHP NCs, two strategies are commonly used, hot injection method and ligand-assisted reprecipitation (LARP) method. The hot injection method has been commonly used for the synthesis of traditional semiconductor NCs. In this type of

synthesis, the precursor solutions containing surface ligands were mixed rapidly at high temperature in inert atmosphere. The precursors react instantaneously after mixture, produces product monomers that forms small nuclei after the concentration reaches the nucleation threshold. The leftover precursors in the solution continues to react and grows on top of the nuclei formed in the previous step. The degree of crystal growth is mostly kinetically controlled, where the chemical reactions are terminated by rapidly cooling of the reaction system.

The hot injection method is soon extended to the synthesis of LHP NPs. Protesescu et al. reported successful synthesis of $CsPbX_3$ NCs with the hot injection method[10], where Cs^+ precursor solution was injected into a precursor solution containing PbX_2 precursors and oleic acid (OA) and oleylamine (OLA) as the surface ligands. The resulting NCs showed cubic shape with sizes in the range of 4-15 nm. As shown in Figure 1a, even though most NCs synthesized were in the weakly quantum confined sizer regime, the emission wavelength was tuned continuously throughout the visible spectral range by synthesis of mixed halide LHP NCs with mixed halide precursors.

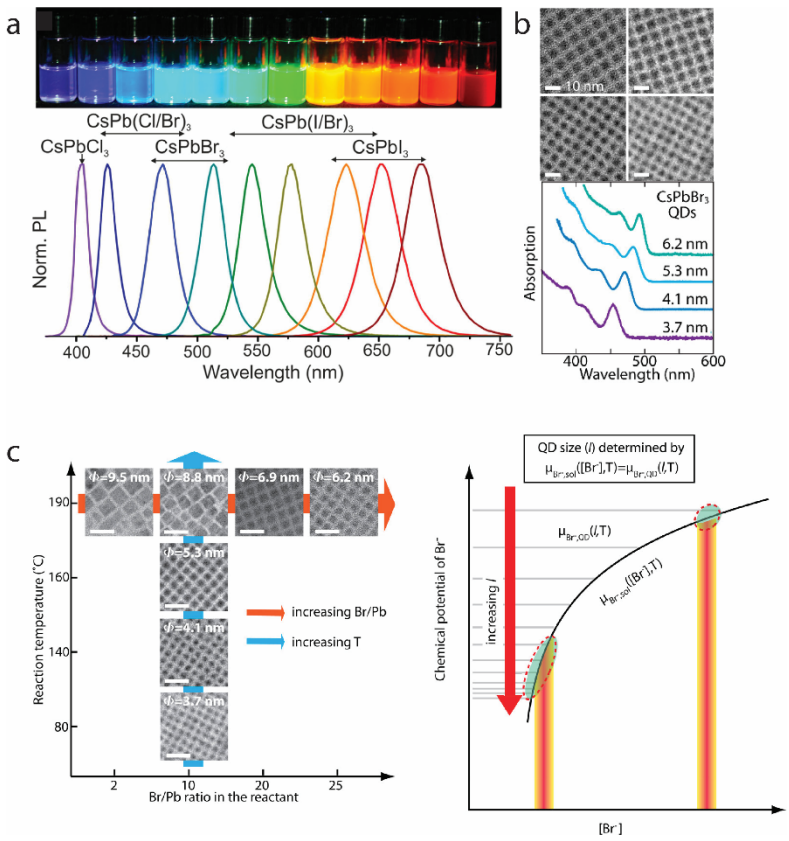

Figure 1 (a) Photos and PL spectra of colloidal perovskite $CsPbX_3$ NCs synthesized by hot injection method. Reprinted with permission from Protesescu, L. et al. *Nano Lett.* **2015**, *15,* 6, 3692–3696. Copyright 2015 American Chemical Society. (b) Absorption, PL spectra and TEM images of $CsPbBr_3$ QDs synthesized with improved hot injection method involving thermodynamic control. (c) Scheme illustrating mechanism of the QD size control using thermodynamic control. (b) and (c) Reprinted with permission from Dong, Y. et al. *Nano Lett.* **2018**, *18*, 6, 3716-3722. Copyright 2018 American Chemical Society.

The hot injection synthetic method of LHP NCs was soon broadened to other LHP NC systems, in terms of both composition and dimensions of the LHP NCs. For instance, Amgar et al. extended the method for the production of LHP NCs with mixed A-site cation

($Cs_xRb_{1-x}PbX_3$), where the resulting NCs also showed spectral tunability by altering the ratio of the two A-site cations[11]. Meanwhile, the synthetic method was not only effective for all inorganic LHP NCs, but also proved applicable for organic-inorganic hybrid LHP NCs. Schmidt et al. For instance, Protesescu et al. also reported synthesis of $FAPbBr_3$ NCs sized around 12 nm and $FAPbI_3$ NCs sized around 10 nm[12, 13]. On the other hand, hot injection method is also applicable for the synthesis of LHP nanomaterials of higher dimensionality. For instance, altering the synthetic protocol for cubic NCs by different reaction conditions leads to the production of $CsPbX_3$ nanoplatelets (NPLs)[14, 15].

In the hot injection method, several factors determine the size and morphology of the resulting NCs, including the ratio of the precursors, the ratio of the surface ligands, the reaction temperature and the reaction time. In order to gain better size control during the synthesis of the LHP NCs, many studies have been carried out with focus on taking snapshots of the reaction mixture during the synthesis, trying to break down the mechanism of the nucleation and crystal growth processes[16-18]. These studies, however, came out with contradictory conclusions, leaving the time scale of the size focusing and defocusing regime still unresolved. Despite the failure to unravel the detailed mechanism of the crystal growth, one certain fact is that the kinetically controlled synthetic method is quite challenging for achieving satisfactory size uniformity for small NCs below 7 nm that are strongly quantum confined.

In an attempt to improve the size uniformity of these small NCs, Dong et al. modified the traditional hot injection synthetic condition by introducing in thermal equilibrium between the dissolved halide salt and halide ions on the NC surface for more

efficient control over the size and morphology of these materials[19]. For this purpose, extreme excess of halide salt was used to push the chemical equilibrium towards stable formation of small sized NCs. As a result, strongly quantum confined $CsPbX_3$ NCs in the size range of 3-7 nm with excellent size distribution and uniform cubic morphology were successfully synthesized, as shown in Figure 1b. The mechanism for the effective size control of the QDs is explained as shown in Figure 1c. Increased chemical potential of Br^- in the solution with higher Br^- concentration lead to increased chemical potential of Br^- on the QD surface after the system reaches thermal equilibrium, which is directly related to the size of the QDs. This work has set the stage for investigation of strongly quantum confined $CsPbX_3$ NCs, whose unique photophysical properties caused by the quantum confinement will be introduced and summarized in the following sections of this chapter.

Apart from the hot injection method, LARP method has been widely utilized in the synthesis of LHP NCs, where the reaction conditions were much gentler, with no strict requirement for high temperature and inert atmosphere. In this type of synthesis, the precursors were dissolved in a polar 'good solvent' and added dropwise into a nonpolar 'poor solvent' containing surface ligands. The precursors will precipitate as the solvent polarity changes upon mixture, leading to nucleation and subsequent crystal growth. Meanwhile, the surface ligands in the 'poor solvent' works as regulators to control the size and morphology of the final products.

Because of the gentle reaction condition, the LARP method has been widely utilized for the synthesis of organic-inorganic hybrid LHP NCs. For instance, Zhang et al. reported successful synthesis of $MAPbX_3$ NPs with LARP method with PbX_2 and MAX

as the precursors, and alkyl amines and carboxylic acids as surface ligands[20]. As shown in Figure 2a, the band gap tunability can be realized by using varied halide precursor ratios. Later, Huang et al. improved the synthetic procedures by using OA and OLA as surface ligands, and tuning the reaction temperature in the range of 0-60 °C[21]. As shown in Figure 2b, the product NCs showed PL peaks in the range of 475-520 nm, corresponding to NC sizes of 1.8-3.6 nm.

Similarly, LARP syntheses of $FAPbX_3$ NCs have been reported many times as well. Weidman et al. reported synthesis of cubic $FAPbX_3$ NCs and $FAPbX_3$ NPLs, with their band gap tunable through altering both the halide composition and the NPL thickness. The morphology of the product was dependent on the halide species, where $FAPbI_3$ were cubic and $FAPbBr_3$ and $FAPbCl_3$ are NPLs, while the thickness of the NPLs were tuned by the ratio of OLA/OA. Similarly, Minh et al. synthesized pure phased cubic $FAPbX_3$ NCs with PbX_2-Dimethyl sulfoxide precursors as well as surface ligand, OLA in the surface solution, rather than in the 'poor solvent'[22]. The size and uniformity of the NCs were tuned by altering the amount of OLA added, where contaminants of NPLs and different size distribution were observed in some reaction conditions, as shown in Figure 2c.

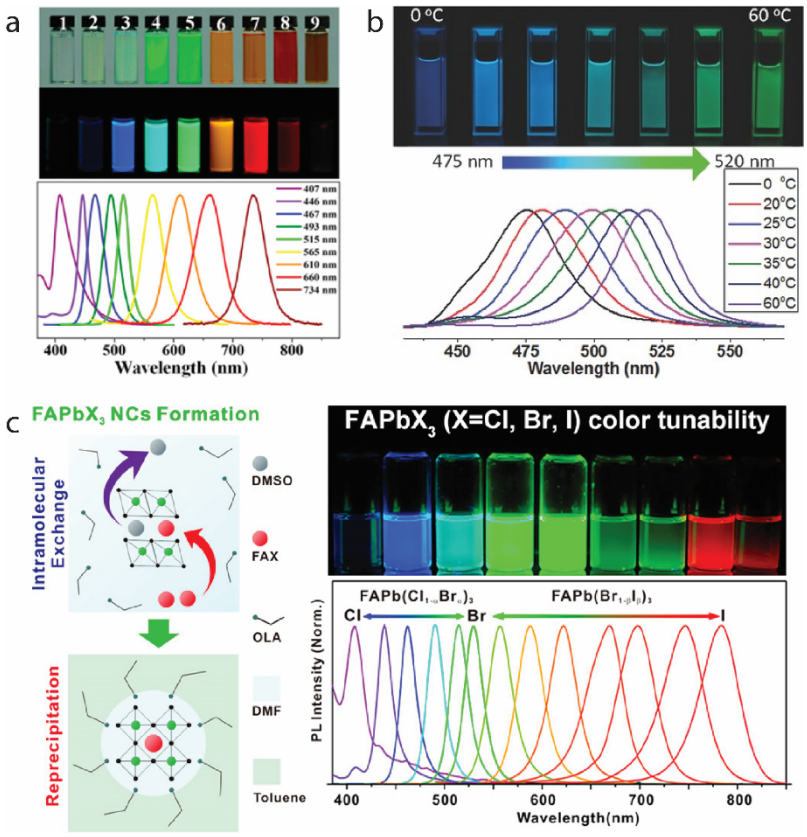

Figure 2 Photos and PL spectra of (a) $MAPbX_3$ NCs synthesized by LARP methods, with tunable band gap controlled by halide composition. Reprinted with permission from Zhang, F. et al. *ACS Nano* **2015,** *9*, 4533-4542. Copyright 2015 American Chemical Society. (b) $MAPbBr_3$ NCs synthesized by LARP methods, with tunable band gap controlled by sizes. Reprinted with permission from Huang, H. et al. *Adv. Sci. (Weinh)* **2015,** *2*, 1500194. Copyright 2015 WILEY-VCH Verlag GmbH & Co. (c) $FAPbX_3$ NCs synthesized by LARP methods, with tunable band gap controlled by halide composition. Reprinted with permission from Minh, D. N. et al. *Chem. Mater.* **2017,** *29*, 5713-5719. Copyright 2017 American Chemical Society.

Despite of the advantages of gentle reaction conditions LARP synthesis can provide, the controllability over the size and morphology of the NCs, especially those of small sizes, remains challenging. This partially results from the complex nucleation and crystal growth kinetics under room temperature condition together with the inefficient control of the solvent mixing process. Thus, for the pursuit of obtaining strongly quantum confined NCs with excellent size uniformity, hot injection methods are more preferable.

2.1.2. Post-synthetic Ligand Exchange of Lead Halide Perovskite Nanocrystals

During the synthesis of LHP NCs, whether with hot injection or LARP approach, long chain organic surface ligands were used for the passivation of the NC surface as well as assist the dispersion of NCs in nonpolar solvent. For current reported synthesis studies, the most commonly used surface ligands were a combination of OLA and OA. These 18-carbon alkyl chain organic ligands bind to the surface of the product NCs through ionic bonds, resulting in the easy desorption of the surface ligand. Loss of the surface ligands exposes the labile bare material not only deteriorate the PLQY, but also greatly impair the structural stability of the NCs, making them prone to dissolve and dissociate and/or aggregate with other NCs. To prevent the ligand loss issue, many researchers have put great efforts on the exploration of surface modification methods.

According to the studies of Weidman et al, the $CsPbX_3$ NCs consisting of PbX_6 building blocks are characterized with a halide-rich surface[23], especially for the strongly quantum confined ones that are synthesized in an environment with excessive amount of halide salt[19]. In this case, oleylammonium halide (OLAX) formed from surface X^- and OLA^+ by ionic bonds was believed to be the surface ligands[24]. The OLAX are relatively

easy to desorb from the NC surface and dissolve in the organic solvents, especially when the samples are purified by polar antisolvent precipitation. The surface modification on the NCs targeting for improved structural stability have been concentrated on undertaking ligand exchange treatment towards surface ligands with stronger binding to the NC surface and bulkier sized to provide increased steric effect for solvent penetration.

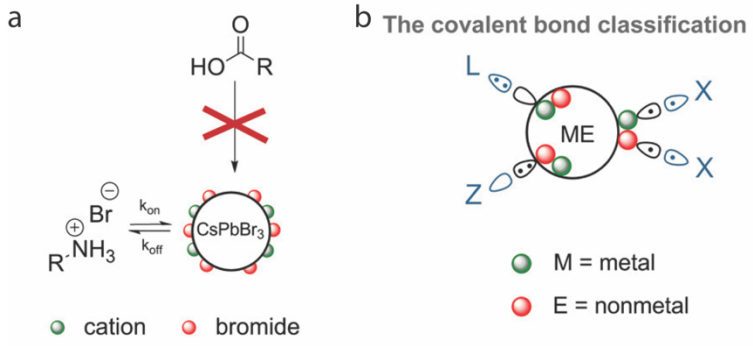

Figure 3 (a) Scheme of oleylammonium bromide (OLAB) binding on surface of $CsPbBr_3$ NCs with a Br- rich surface. (b) Schemes of classification of different bond types. Reprinted with permission from De Roo, J. et al. *ACS Nano* **2016,** *10*, 2071-2081. Copyright 2016 American Chemical Society.

One of the commonly employed surface treatment methods for improved NC stability is to carry out ligand exchange treatment with didodecyldimethylammonium halide (DDAX)[25]. Compared to the original OLAX surface ligands that binds to the NC surface in an ionic fashion, as illustrated in Figure 3a, DDAX molecules binds to the surface covalently as X-type ligands, as described in Figure 3b, where the binding is predicted and proved to be more robust[24, 26]. Moreover, DDAX molecules with two 12-

carbon alkyl chains also provides larger coverage on the LHP NC surfaces compared to OLAX molecules, reducing the encounter of bare NCs with polar solvent or humidity that will dissolve the NCs. The replacement of surface ligands to bulkier molecules greatly improves the stability of the NCs, especially when the NCs are in conditions where the ligand desorption is more likely, such as during purification with polar solvents and in low concentration solutions. Similarly, utilization of hexylphosphonate as a X-type ligands for the passivation of LHP NCs proved capable to increase the NC stability[27].

While the bulky organic surface ligands like DDAX and alkyl phosphonate greatly improves NC stability, the high surface coverage these materials provide are not always desired for all scenarios. Since the bulky organic surface ligands inevitably increase the inter-NC distances with insulating media, they hinder the charge carrier mobility required for LEDs and photovoltaic devices. For this reason, efforts have been made to modify the NC surface with ligands either conducting or reducing the inter-NC distances. For the prior strategy, surface ligands that promotes delocalization of electrons and holes can be used. For instance, some studies showed that incorporation of aromatic ligands, such as benzylamine and benzoic acid, improves the conductivity of LHP NC films by π-conjugation between the overlapping ligand molecules[28]. Meanwhile, for the latter strategy, small metal cations that binds to the lattice strongly, such as sodium[29] and potassium[30], have been used to replace the original OLAX surface ligands. The resulting NCs showed improved stability as well as improved conductivity.

More recently, smaller zwitterionic ligands have become increasingly explored. This type of molecules is characterized by containing two functional groups with opposite

charges that can bind to surface ions of different charges, greatly increasing their binding strength. The resulting NCs after the ligand exchange have shown remarkably improved stability, being able to remain their structural integrity and a relatively high PLQY even after extensive purification by antisolvent precipitation method[31].

2.2. Photophysical Properties of Lead Halide Perovskite Nanocrystals

Thanks to the advances of the synthetic protocols for strongly quantum confined LHP NCs of different nature with controllable size and morphology, size and component dependent photophysical properties of these NCs can now be explored by spectroscopic methods. In this section, research findings on the size and composition dependent photophysical properties of LHP NCs are going to be discussed and summarized.

2.2.1. Optical Band Gap: Absorption and Emission

The most straightforward size and compositional dependent optical property of LHP NCs is the absorption and emission energy, corresponding to electronic transitions between the valence and conduction bands. LHP materials are direct band gap materials, whose band edge states consist of the molecular orbitals formed from bonding between the Pb and halides. Specifically, the conduction band forms from the antibonding orbital of the Pb 6p orbitals and halide np orbitals, while the valence band forms from the antibonding orbital of the Pb 6s orbitals and halide np orbitals. As a result, altering the halide species in LHP materials changes the absorption and emission spectral ranges of the materials, with increasing band gap as the halide changes from Cl^- to Br^- to I^-. Meanwhile, changing the A-site cations between Cs^+, MA^+ and FA^+ does not result in significant changes in the band gap since they are not directly involved in the molecular

orbital formation. Their limited modification on the band gaps results from the changes in the lattice parameters from steric effects, where larger A-site cations corresponds to NCs with lower band gap[32].

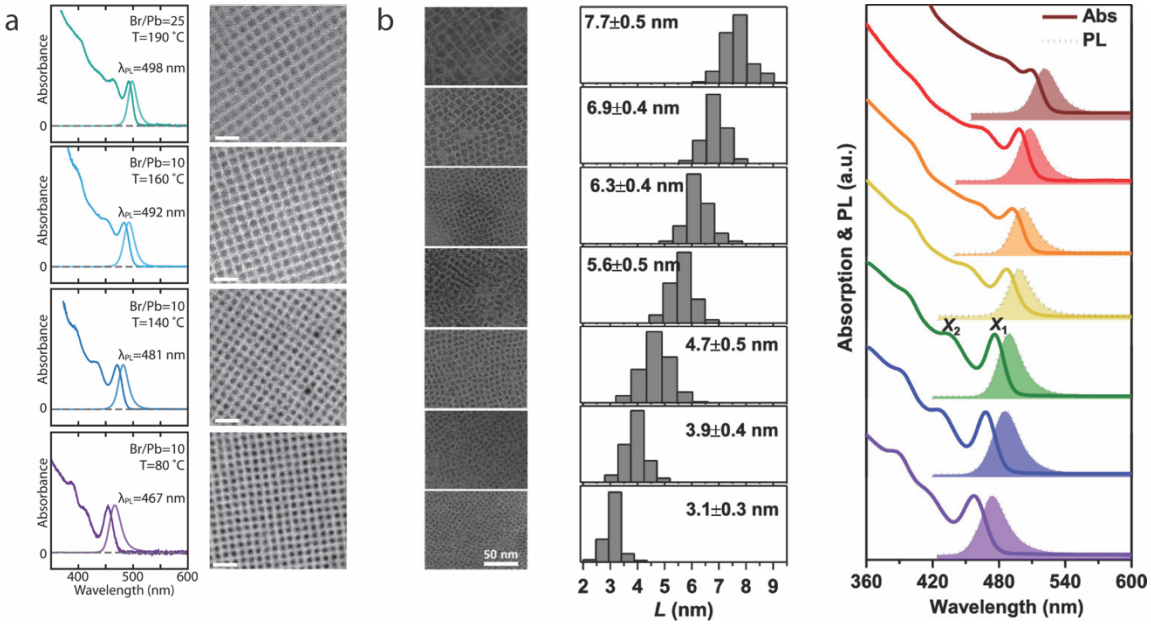

Figure 4 (a) TEM images and absorption/PL spectra of $CsPbBr_3$ QDs of sizes in the range of 3.7-6.2 nm. Reprinted with permission from Dong, Y. et al. *Nano Lett.* **2018**, *18*, 6, 3716-3722. Copyright 2018 American Chemical Society. (b) TEM images and absorption/PL spectra of $FAPbBr_3$ QDs of sizes in the range of 3.1-7.7 nm. Reprinted with permission from Li, Y. et al. *Chem. Mater.* **2019**, *32*, 549-556. Copyright 2019 American Chemical Society.

On the other hand, similar to all other types of quantum confined materials, the size dependence band gap is the direct result of quantum confinement, especially for those

in the strong quantum confinement regime, where their dimensions are smaller than the exciton Bohr diameter, which is 5 nm, 7 nm and 12 nm for $CsPbCl_3$, $CsPbBr_3$ and $CsPbI_3$, respectively[10]. In the case of strong quantum confinement, the smaller the volume where the excitons are spatially confined to, the more blueshift is going to be observed in the absorption and emission spectra of the LHP materials. In LHP materials, more reports on the size dependence of absorption/emission peak have been produced on the NPLs, where the thickness control have been more well developed[14, 33, 34].

More recently, more research reports showed successful control over the sizes of $CsPbBr_3$ and $FAPbBr_3$ QDs, where blueshifts in absorption and emission spectra were also observed for QDs of smaller sizes[19, 35]. As shown in Figure 4, $CsPbBr_3$ and $FAPbBr_3$ QDs both exhibited redshift in both absorption and emission peak positions when their sizes increase from ~3 nm to ~7 nm. Band gap changes due to decreasing sizes observed in these two materials are expected since their sizes are well below the exciton Bohr diameter (7 nm) and are thus in the strongly quantum confinement regime.

Apart from the absolute value of absorption and emission peak in $CsPbBr_3$ QDs, the difference between the two, or Stokes shift, is also reported to be dependent on the QD sizes[36]. As shown in Figure 5a, when the sizes of the QDs increases from 3.8 to 12.8 nm, a monotonic decrease of the Stokes shift was observed from 82 to 20 meV. This was explained by the existence of a size dependent confined hole state above the valence band edge, as illustrated in Figure 5b, where the energy difference between the confined hole state and the valence band edge is one of the sources for the Stokes shift. The size

dependent Stokes shift is also observed in the other papers mentioned above where strongly quantum confined $CsPbBr_3$ and $FAPbBr_3$ QDs were synthesized[19, 35].

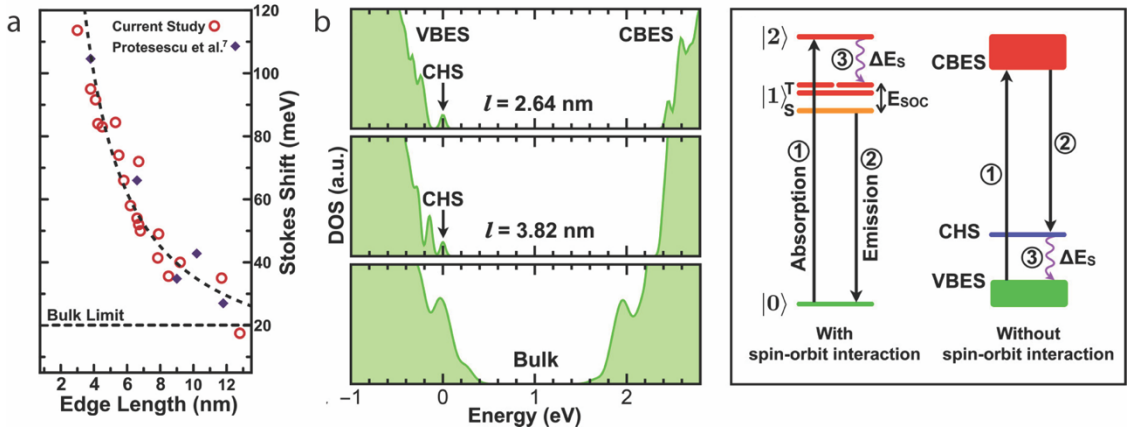

Figure 5 (a) Stokes shift of $CsPbBr_3$ QDs with sizes in the range of 3.8-12.8 nm. (b) Density of states (DOS) calculated for $CsPbBr_3$ QDs and schematic mechanism of size dependent Stokes shift. (a) and (b) Reprinted with permission from Brennan, M. et al. *J. Am. Chem. Soc.* **2017**, *139*, 2201-12208. Copyright 2017 American Chemical Society.

2.2.2. Exciton Fine Structure: Energetics and Dynamics

Excitons are the main forms of charge carriers in LHP NCs after excitation, especially for the case of strong quantum confined NCs. The degeneracies of the lowest excitonic states are split into several sublevels, or exciton fine structure, as the result of the combined effect of the short- and long-range exchange interactions, spin-orbit coupling, intrinsic crystal field, and shape anisotropy. More specifically, they are classified as bright and dark exciton, based on whether their direct transition to the ground state is optically active. In traditional semiconductor QD materials such as CdSe, the

lowest excitonic states are found to be the optically inactive dark exciton state. And the energy difference between the bright and dark exciton state, bright-dark energy splitting (ΔE_{BD}), is observed to increase with decreasing QD sizes[37, 38].

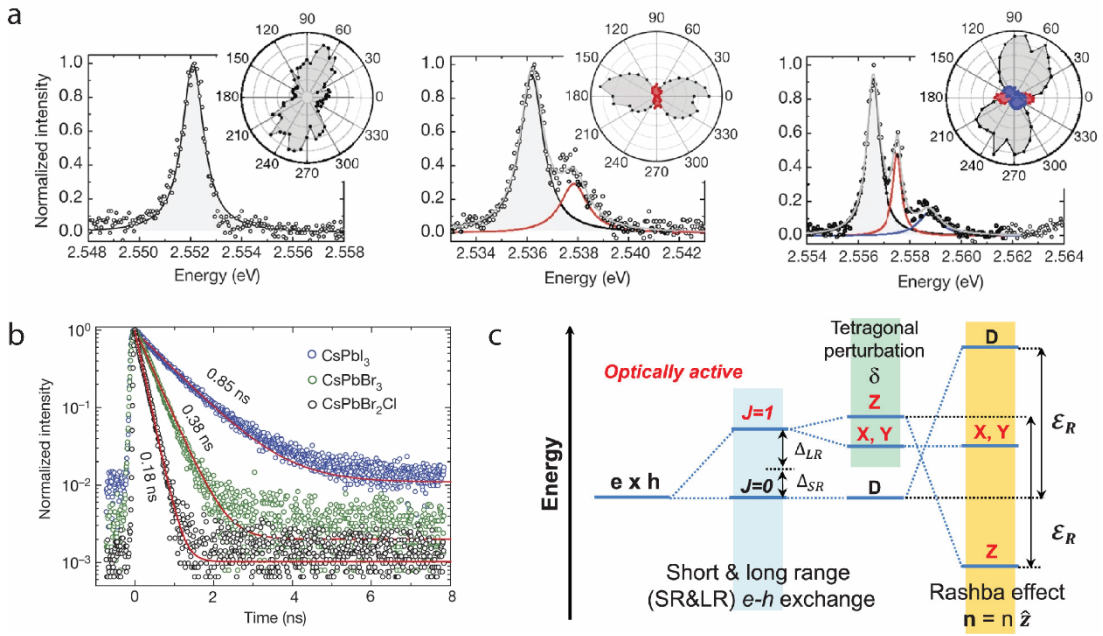

Figure 6 (a) PL spectra of weakly quantum confined $CsPbBr_2Cl$ NCs with different polarizations, showing degeneracies of the bright triplet exciton emissions. (b) Time resolved PL intensity of weakly quantum confined $CsPbX_3$ NCs showing only fast decaying components. (a) and (b) Reprinted with permission from Becker, M. A. et al. *Nature* **2018**, *553*, 189-193. Copyright 2018 Springer Nature. (c) Scheme of the exciton fine structure of weakly quantum confined $CsPbX_3$ NCs. Reprinted with permission from Sercel, P. C. et al. *Nano Lett.* **2019**, *19*, 4068-4077. Copyright 2019 American Chemical Society.

In contrast, recent studies on the exciton fine structures in weakly quantum confined $CsPbX_3$ NCs reported bright triplet exciton states as the lowest exciton states with sub-ns exciton lifetime, as shown in Figure 6a and b. This observation makes LHP NCs the first semiconductor materials reported to have a bright ground exciton state[39]. This unusual exciton level ordering reversal was attributed to the Rashba effect, which was confirmed by following computational and experimental study[40, 41]. The computational study depicts the exciton fine structure of LHP NCs as in Figure 6c, with a singlet dark exciton state as the lowest level and a triplet bright exciton state as the higher level with only electron-hole exchange interaction, and a level ordering reversal in the presence of the Rashba effect, where the lowest exciton states become the 3-fold degenerate bright exciton states.

However, the level order reversal observed in weakly quantum confined $CsPbX_3$ NCs is reported to be reverted when the inversion symmetry of the NC is broken. For instance, emission from the dark exciton state with redshifted peak position compared to the bright exciton states were observed in the case where magnetic field was applied to the $CsPbX_3$ NCs[42, 43]. With increasing magnetic field strength, the proportion of the dark exciton also increases. Similarly, the level ordering reversal is observed in the case where the A-site cation is replaced with organic cation, FA^+. As shown in Figure 7a and b, the lowest level emission from dark exciton states with prolonged lifetime was observed in weakly quantum confined $FAPbX_3$ NCs under magnetic field[44, 45]. In the same research, ΔE_{BD} was compared between LHP NCs of different components, in terms of both a-site

cations and halide anions. The $FAPbBr_3$ NCs showed a decreased ΔE_{BD} compared to the $CsPbBr_3$ NCs, as a result of increased charge screening with the presence of an organic cation. Meanwhile, the ΔE_{BD} of $CsPbX_3$ NCs showed an increasing trend when the halide is altered from I^- to Br^- to Cl^-, corresponding to the increasing optical band gap in these NCs, respectively.

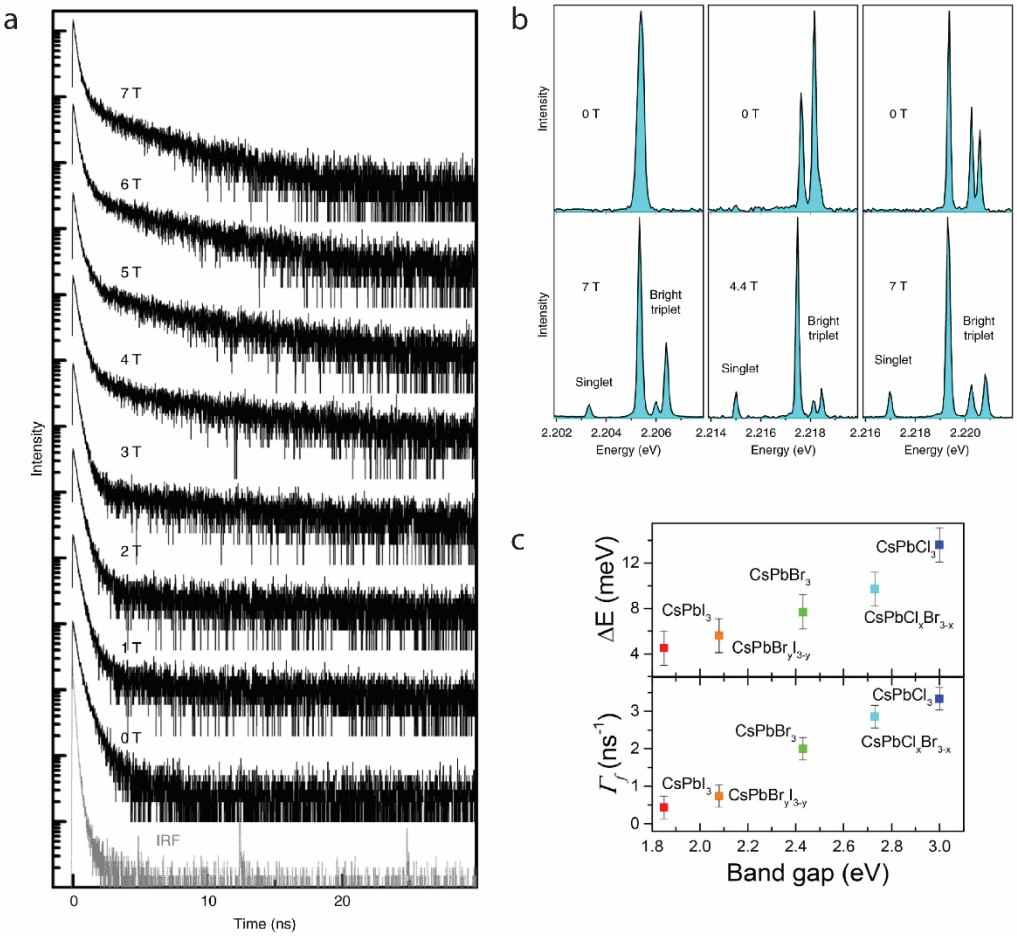

Figure 7 (a) Time resolved PL intensity of weakly quantum confined $FAPbBr_3$ NCs under magnetic fields. (a) PL spectra of weakly quantum confined $FAPbBr_3$ NCs showing degeneracies of the bright triplet exciton and dark singlet exciton emissions. (a) and (b)

Reprinted with permission from Tamarat, P. et al. *Nature Mater.* **2019**, *18*, 717-724. Copyright 2019 Springer Nature. (c) Bright-dark energy splitting and fast component decay rate in weakly quantum confined $CsPbX_3$ NCs with different halides. Reprinted with permission from Chen, L. et al. *Nano Lett.* **2018**, *18*, 2074-2080. Copyright 2018 American Chemical Society.

(Figure 7 continued)

As shown in Figure 8a, the electron-hole exchange interaction is greatly enhanced for strongly quantum confined LHP NCs, predicted by the computational study, the dark exciton state will become the lowest exciton state. This is confirmed by recent experimental studies on the $CsPbBr_3$ NCs, whose results are shown in Figure 8b, where intense dark exciton emission situated redshifted to the bright exciton emission energy is observed, with extremely long μs scale lifetime[8, 45]. The observations are applicable not only to 4 nm strongly quantum confined cubic QDs, but also to 2nm thick nanowires (NWs) and NPLs. For these strongly quantum confined NCs, ΔE_{BD} was observed to be in the range of 17-22 meV, about one order of magnitude larger compared to previous observations in the weakly quantum confined NCs. In a later report, detailed studies on the dark exciton emission properties further justifies the size dependence of the dark exciton lifetime and ΔE_{BD}[46], confirming the conclusions of the computational study.

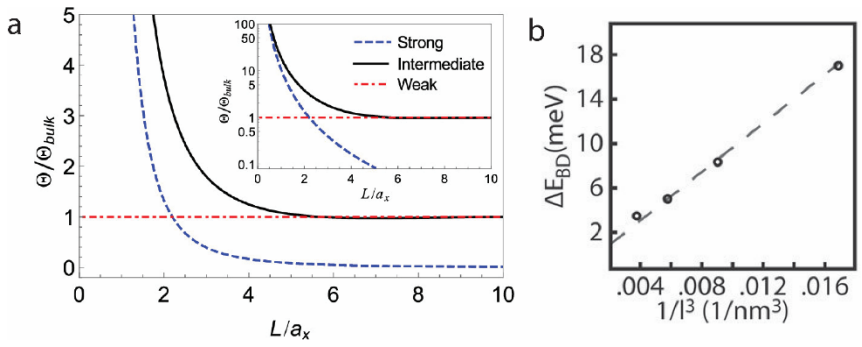

Figure 8 (a) Computational results of the electron-hole exchange interaction factor of $CsPbBr_3$ NCs of different sizes. Reprinted with permission from Sercel, P. C. et al. *Nano Lett.* **2019**, *19*, 4068-4077. Copyright 2019 American Chemical Society. (b) Experimental results of bright-dark energy splitting in $CsPbBr_3$ NCs of different sizes. Reprinted with permission from Rossi, D. et al. *J. Chem. Phys.* **2020**, *153*, 184703. Copyright 2020 AIP Publishing.

2.2.3. Electron-Phonon Coupling: Temperature Dependent Photoluminescence

In solid state physics, phonons describe the collective vibrations of the lattice atoms and molecules with certain frequencies. The interaction of charge carriers with phonons in semiconductor materials have a significant impact on the carrier mobility as well as the spectral features, such as the emission peak energy and linewidth. The contribution of electron-phonon coupling to the PL linewidth is intriguing for researchers because of their large contribution to the emission quality of LHP NCs as photon sources. The electron-phonon coupling is intensively investigated through measurements of temperature dependent PL spectroscopy, as the phonon scattering is heavily dependent on

temperature. The linewidth broadening can be fitted to the Segall model, expressed by the following equation[47]:

$$\Gamma(T) = \Gamma_{inh} + \gamma_{ac}T + \gamma_{LO}\frac{1}{e^{E_{LO}/k_bT} - 1}$$

(Eq. 1)

In this model, the linewidth, Γ(T), has three major contributions: inhomogeneous broadening, Γ_{inh}, scattering of acoustic phonon, $\gamma_{ac}T$, and scattering of longitudinal optical (LO) phonon, $\gamma_{LO}\frac{1}{e^{E_{LO}/k_bT}-1}$. As shown in this equation (Eq. 1), the contribution of acoustic phonon scattering is linearly proportional to the temperature, while the contribution of LO phonon scattering is exponentially related to the temperature. Thus, in the lower temperature range (below 50 K), the dominant scattering is with acoustic phonon, and in the higher temperature range (above 50 K), the dominant scattering is with LO phonon.

Temperature dependent PL measurements on weakly quantum confined $CsPbX_3$ NCs observed a general blue-shifting trend of the PL peak as temperature increases, with the exception of $CsPbCl_3$ NCs showing a redshift of the PL peak as temperature increases in the range of 200-300 K[48-52]. The temperature dependent peak energy is attributed to a combined effect of lattice dilation, electron phonon coupling and phase transitions. Meanwhile, the temperature dependent linewidth showed a monotonous increase as the temperature increases. Fitting the temperature dependent linewidth of the $CsPbCl_3$ NCs in the single nanocrystal study to the model mentioned above (Eq. 1) results in LO phonon coupling strength, γ_{LO}, in the range of 21-60 meV, and negligible contribution of the acoustic phonon[49]. The comparative study between $CsPbX_3$ NCs with different halide

anions showed increasing phonon coupling strength, γ_{ac}, from I^- to Br^- to Cl^-, and significant smaller γ_{LO} in $CsPbI_3$ NCs as compared to $CsPbCl_3$ and $CsPbBr_3$ NCs[48].

For hybrid LHP NCs with an organic A-site cation, additional phonon modes with higher energies than in all-inorganic LHP NCs (above 18 meV) were reported[53-55], which are associated with the vibrational modes of the organic molecules. To see if these additional phonon modes impact the PL linewidth broadening, temperature dependent PL measurements were carried out on $MAPbI_3$, $MAPbBr_3$, $FAPbI_3$ and $FAPbBr_3$ NCs[54, 56-58]. While the $MAPbX_3$ NCs showed huge jumps in both the temperature dependent peak energy and linewidth due to phase transitions, $MAPbX_3$ $FAPbX_3$ NCs showed similar trends as observed in all-inorganic $CsPbX_3$ NCs. Quantitatively, the parameters extracted from the linewidth broadening model (Eq. 1) showed that both the LO phonon energy and the LO phonon coupling strength are comparable in all three materials, showing that the higher energy phonon modes in hybrid LNP NCs are not involved in the PL linewidth broadening.

Apart from compositions of the LHP NCs, the impacts of the sizes of the NCs on the PL linewidth broadening are also explored by temperature dependent PL study[9]. In this study, the measurements were carried out on strongly quantum confined $CsPbBr_3$ QDs with sizes in the range of 3.9-6.3 nm. The temperature dependent PL peak energy and linewidth follow the same trends as in their weakly quantum confined counterparts. However, the fitting results to the linewidth broadening model (Eq. 1) showed significant size dependence. The LO phonon coupling strength increased by almost 3-folds as the QD sizes decreases from 6.3 nm to 3.9 nm, while the acoustic phonon coupling strength

decreased as the QD sizes decreases. The reason for the strongly size dependent phonon coupling strengths are proposed to be related to the phonon coupling assisted by surface ligands, which are more dominant in smaller QDs.

In summary, this section reviews the synthesis and post-synthetic ligand exchange on strongly quantum confined LHP NCs, followed by their photophysical properties. The photophysical properties, such as band gap, exciton fine structure and electron phonon coupling are reported to show some dependence on the size and component. In the following chapters, the size and component dependent photophysical properties will be extended into more LHP NC systems, such as strongly quantum confined $FAPbBr_3$ NCs and electronically coupled ensembles of $CsPbBr_3$ NCs.

3. CHAPTER III

EXCITON PHOTOLUMINESCENCE OF STRONGLY QUANTUM-CONFINED FORMAMIDINIUM LEAD BROMIDE QUANTUM DOTS*

3.1. Introduction

Metal halide perovskite (MHP) semiconductor nanocrystals (NCs) have attracted much attention in photonic and photovoltaic applications[1-3, 6, 59-63] for their superb photon emitting and charge carrier transporting properties outperforming many existing semiconductor NCs.[64-66] In contrast to traditional semiconductor NCs, where the quantum confinement of exciton has been extensively utilized to tune the bandgap and the energetics of the charge carriers, chemical tuning of the bandgap without resorting to the quantum confinement has been the main approach for MHP nanocrystals.[10, 67, 68] Facile exchange of halide ions with continuously variable composition within the lattice of MHP NCs allowed for continuous tuning of the bandgap and exciton transition energy independently of the quantum confinement. For this reason, many applications of MHP NCs that utilized emission of photons or transport of charge carriers of varying energy did not require quantum confinement.

On the other hand, the quantum confinement affects not only the energy of the emitted photons and charges derived from the photoexcited exciton in quantum dots

---

(QDs), but also other properties that are sensitive to spatial confinement. Fine structure of the manifold of bright and dark exciton states[38, 41], inter-QD electronic coupling in the QD solids and arrays[69-71], and the intra-QD sensitization by exciton[72-75] are among those affected by the quantum confinement, which also modifies the energy of the emitted photon. With progress in the methods of synthesizing strongly confined MHP QDs[19, 76], the photoluminescence (PL) from dark lowest-energy exciton state was recently observed in strongly confined $CsPbBr_3$ QDs[8], contrasting to weakly confined $CsPbBr_3$ NCs having the bright lowest-energy exciton state[39]. The inversion of the relative energy levels of the bright and dark states determined by the size-dependent exchange energy of electron and hole was considered responsible for the difference between the weakly and strongly confined $CsPbBr_3$ NCs[41]. Auger decay of exciton is another process that is highly dependent on the size of the QDs, with the bi-exciton lifetime following a universal volume scaling.[35, 77, 78]

So far, studies in strongly quantum-confined MHP QDs have been performed more in fully inorganic MHP systems compared to the hybrid MHP systems with organic A-site cation that exhibit several unique features absent in fully inorganic MHP systems. In bulk and non-confined hybrid MHP, the role of librational motion of the organic cations such as methylammonium (MA^+) or formamidinium (FA^+) ion on the charge carrier screening and its effect on the charge carrier transport have been studied extensively.[79-83] The coupling of exciton transition with the internal nuclear motions of the organic cation is another phenomenon unique to the hybrid MHP systems that is absent in fully inorganic MHP NCs.[53]

In this work, we synthesized strongly quantum-confined $FAPbBr_3$ QDs and investigated their exciton PL spectra and relaxation dynamics at various temperatures and external magnetic fields. In addition to examining the quantum confinement effect on exciton transition energy at the ambient temperature, information on exciton fine structure was also obtained from the dynamic exciton PL spectra at 5 K and under external magnetic field. We also compared the results from $FAPbBr_3$ QDs with those of fully inorganic $CsPbBr_3$ QDs in the similar size range from the earlier studies to examine the similarities and differences between the two strongly quantum-confined MHP QDs.

3.2. Experimental Methods

3.2.1. Synthesis of $FAPbBr_3$ QDs

$FAPbBr_3$ QDs in the size range of 3.6-6.2 nm were synthesized using the procedure modified from the previously reported method for the synthesis of larger $FAPbBr_3$ NCs in weakly confined regime.[12] Modifications were made to the reaction temperature, preparation of the precursor solutions and the product purification to control the size in the strongly confined regime. Briefly, Br precursor was prepared by dissolving oleylammonium bromide (OLAB, 200 mg) in 2 mL of 1-octadecene (ODE) at 120 °C under N_2 atmosphere after degassing at 120 °C for 30 minutes on a Schlenk line. FA/Pb precursor was prepared by dissolving lead acetate trihydrate (76 mg) and formamidinium acetate (80 mg) in the mixture of ODE (8 mL) and oleic acid (OA, 2mL) under N_2 atmosphere after degassing at 120 °C for 30 minutes. The Br precursor solution was rapidly injected into the FA/Pb precursor solution to initiate the reaction at each given reaction temperature (80-130°C) that produced the QDs of different size. After 30 seconds

of reaction, the reaction was quenched by rapidly cooling the reactant mixture to 40 °C with an ice-water bath. The reaction product was centrifuged to remove the unreacted salt. The product QDs in the supernatant were recovered by precipitation with methyl acetate and subsequently redispersion in hexane. The average size of the QDs was determined from the TEM images obtained with FEI Tecnai G2 F20 ST FE-TEM at 200 kV.

3.2.2. Spectroscopic characterization

Steady state absorption and PL spectra of the QDs dispersed in hexane were obtained with an Ocean Optics CCD spectrometer (USB2000 or QE65). PL quantum yield of the QDs solutions at room temperature was measured using quinine sulfate in 0.05 M sulfuric acid as the reference with known quantum yield of 54%, and evaluated with 350 nm excitation. PL lifetime of the QD solutions at room temperature was measured using a time-correlated single photon counting setup (PicoHarp 300) equipped with an avalanche photodiode (MPD PDM series) under 50 ps pulsed excitation at 405 nm (PicoQuant, P-C-405). Temperature-dependent steady state PL spectra of the QDs were obtained using an open-cycle optical cryostat (Janis ST-100) under 405 nm cw excitation (RGBLase, FBB-405-200-FM-E-1-0). Time-resolved PL spectra of the QD samples at 5 K were obtained in an open-cycle cryostat (Oxford Instruments Microstat-HE) using a streak camera (Hamamatsu, C14831) coupled to an imaging spectrograph (Princeton Instruments, Acton SpectraPro SP-2300) under 405 nm, 45 ps pulsed excitation (Horiba, 45 ps). Time-dependent PL intensities under the magnetic field were measured in a magneto-optical cryostat (Cryovac) with 0-8 T of magnetic field provided by a superconducting magnet under Faraday geometry. For this measurement, the QD samples

were excited with 405 nm, 150 ns pulses and the time-dependent PL intensities were recorded with a time-correlated single photon counting instrument (PicoHarp 300). For all the measurements made in the cryostat, QDs imbedded in polystyrene (PS) matrix were used, which were prepared by drop-casting QDs dispersed in PS/toluene solution (1 % PS by weight) on a sapphire window and drying under vacuum.

3.3. Results and Discussion

Figure 9 shows the TEM images, absorption and PL spectra, and time-dependent PL intensity of strongly quantum-confined $FAPbBr_3$ QDs of varying sizes dispersed in hexane at room temperature. Table 1 summarizes the average size of the QDs, exciton absorption and PL peak, and the PL lifetime for all $FAPbBr_3$ QDs shown in Figure 9. The TEM images show that all the QDs studied here have approximately a cubic morphology with size distribution of < 5 %, as summarized in Figure 10. The reaction temperature that was varied to control the size is indicted in each panel showing the absorption and PL spectra. Both exciton absorption and PL peaks show a blueshift with decreasing QD size resulting from the quantum confinement, since the size of the QDs are smaller than twice of the reported exciton Bohr radius of ~3.5 nm[84]. The room-temperature PL data show a single-exponential decay with the lifetimes in the range of 6.3 - 6.7 ns and the PL quantum yield of ~65 % for all $FAPbBr_3$ QDs studied here, exhibiting a relatively weak size dependence. The radiative lifetime estimated from the PL lifetime and PL quantum yield is ~10 ns for these QDs, which is much shorter than ~30 ns radiative lifetime reported in the weakly or non-confined NCs.[12]

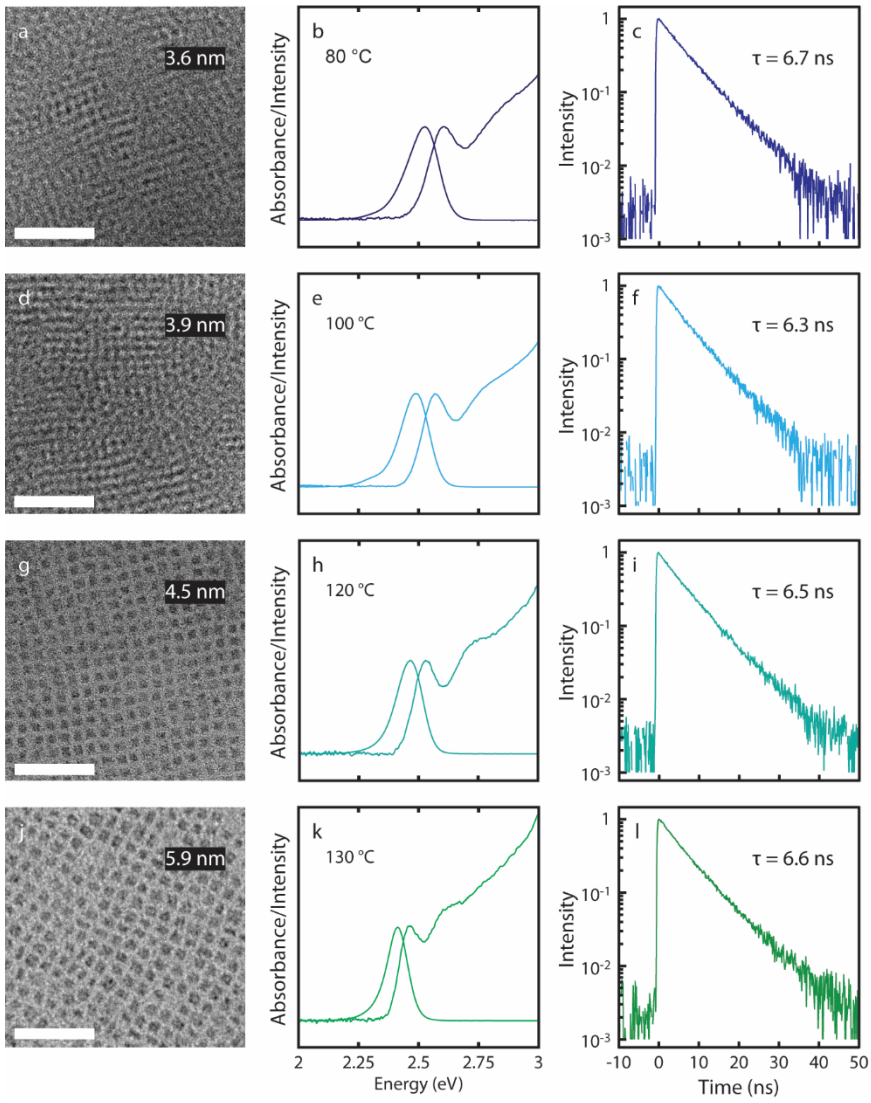

Figure 9 TEM images (left panels), absorption and PL spectra (middle panels) and time-dependent PL intensities (right panels) of $FAPbBr_3$ QDs of different sizes: (a, b, c) 3.6 nm, (d, e, f) 3.9 nm, (g, h, i) 4.5 nm, (j, k, l) 5.9 nm. Scale bars in the TEM images are 50 nm. Reprinted with permission from Tang, X. et al *J. Phys. Chem. C* **2022**, *126*, 18366-18373. Copyright 2022 American Chemical Society.

Table 1 Average QD size, absorption and PL peak and PL lifetime at room temperature. E_{abs} and E_{PL} are the energy of the absorption and PL peak respectively. τ is the single-exponential decay time constant of the PL. Reprinted with permission from Tang, X. et al *J. Phys. Chem. C* **2022**, *126*, 18366-18373. Copyright 2022 American Chemical Society.

QD size	**E_{abs}**	**E_{PL}**	**τ**
3.6 nm	2.62 eV	2.53 eV	6.7 ns
3.9 nm	2.58 eV	2.49 eV	6.3 ns
4.5 nm	2.54 eV	2.46 eV	6.6 ns
5.9 nm	2.47 eV	2.41 eV	6.5 ns

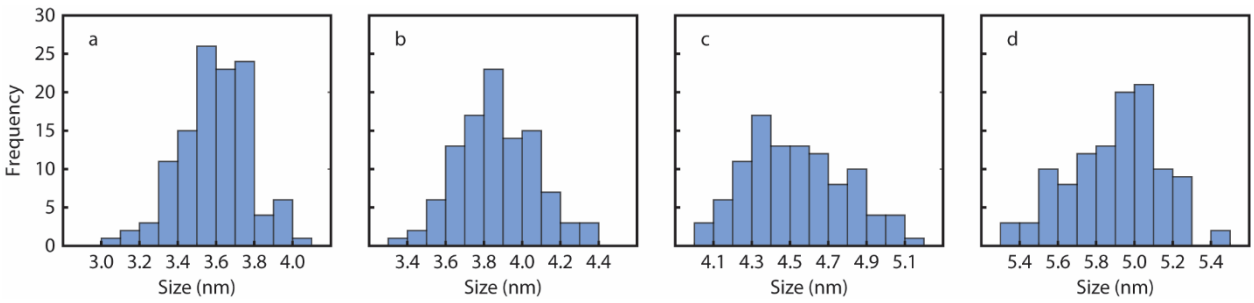

Figure 10 Histogram of the edge-to-edge length of $FAPbBr_3$ QDs of different average sizes. Each histogram was obtained by analyzing more than 100 QDs. The edge-to-edge length was determined from the TEM line profile. Reprinted with permission from Tang, X. et al *J. Phys. Chem. C* **2022**, *126*, 18366-18373. Copyright 2022 American Chemical Society.

The size-dependent bandgap of $FAPbBr_3$ QDs is compared to that of $CsPbBr_3$ QDs in the same size ranges reported in the earlier study[19] in Figure 11. The bulk bandgap of $CsPbBr_3$ and $FAPbBr_3$ QDs are similar, 2.36 eV and 2.29 eV respectively, since the band edge levels are mainly composed of the molecular orbitals of Pb nonbonding and Pb-Br antibonding orbitals.[85] The variation of the exciton absorption peak with the size relative to the bulk bandgap shown in Figure 11 is also very similar in both $CsPbBr_3$ and $FAPbBr_3$ QDs. This similarity between $FAPbBr_3$ and $CsPbBr_3$ QDs is expected considering their close exciton Bohr radii of ~3.5 nm[10, 84] and only moderate difference in the dielectric constants (ε_r ~5 in $CsPbBr_3$ QDs and ε_r ~8.6 in $FAPbBr_3$ QDs).[10, 84, 86] In large non-confined size regime, the presence of polaronic confinement of exciton has been suggested in $CsPbBr_3$ NCs although it is unclear whether $FAPbBr_3$ NCs behave similarly to $CsPbBr_3$ NCs[87].

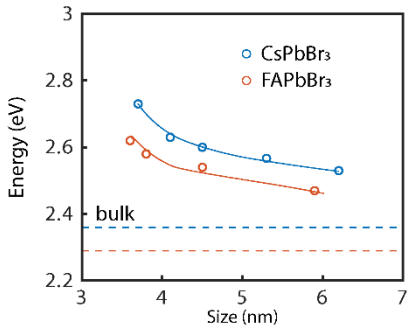

Figure 11 Size-dependent exciton absorption peak energy of CsPbBr3 QDs (blue) and $FAPbBr_3$ QDs (red). Reprinted with permission from Tang, X. et al *J. Phys. Chem. C* **2022**, *126*, 18366-18373. Copyright 2022 American Chemical Society.

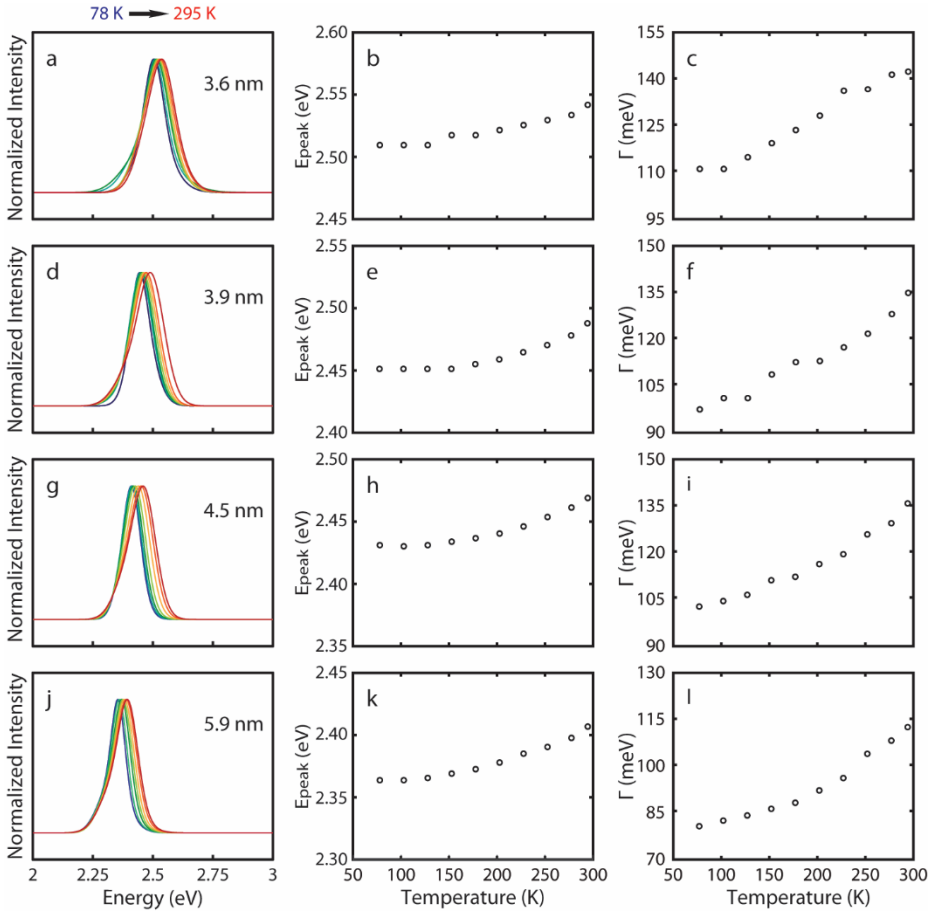

Figure 12 Temperature-dependent PL spectra (left panel), PL peak energy (E_{peak}, middle panel), and full width at half maximum (Γ, right panel) of $FAPbBr_3$ QDs of different sizes in the temperature range of 78-295 K. The sizes of the QDs are indicated in the panels showing the PL spectra. Reprinted with permission from Tang, X. et al *J. Phys. Chem. C* **2022**, *126*, 18366-18373. Copyright 2022 American Chemical Society.

Figure 12 shows the temperature-dependent steady state PL spectra of $FAPbBr_3$ QDs embedded in polystyrene (PS) matrix in the temperature range of 78-295 K. Temperature-dependent PL peak energy (E_{peak}) and full width at half maximum (Γ) are

also plotted next to the PL spectra. $FAPbBr_3$ QDs of all sizes studied here show a continues and monotonous redshift of E_{peak} with decreasing temperature, which reflects the temperature-dependent bandgap affected by the lattice dilation and electron-phonon coupling[88]. $FAPbB_3$ QDs exhibit the redshift of E_{peak} down to ~150 K and becomes much less sensitive to the temperature below ~150 K with no sign of phase transition in the PL spectra previously reported for bulk films[54]. The temperature-shift of E_{peak} in strongly quantum-confined $FAPbB_3$ QDs generally mirrors that of the larger non-confined $FAPbB_3$ NCs reported previously[54, 56] with no particular effect of strong confinement. Compared to $CsPbBr_3$ QDs in the similar size range studied recently[9], $FAPbBr_3$ QDs exhibit more monotonous temperature dependence of E_{peak}. In $CsPbBr_3$ QDs, dE_{peak}/dT changed the sign at ~200 K that was interpreted as the result of different contributions of acoustic and optical phonons to the electron-phonon coupling having the opposite signs of dE_{peak}/dT[48]. Such inversion of the sign of dE_{peak}/dT is absent in $FAPbBr_3$ QDs. The temperature-dependent Γ of the PL spectra contributed by the inhomogeneous broadening and electron-phonon coupling shows generally larger values for the smaller QDs, which has also been observed in other QDs including $CsPbBr_3$ QDs and II-VI QDs.[9, 89] Overall, the size- and temperature-dependent Γ of the PL from $FAPbBr_3$ QDs does not deviate much from typical behavior expected from the colloidal semiconductor QDs.

In previous studies of $CsPbBr_3$ QDs, imposing a strong quantum confinement modified the exciton fine structure, notably pushing the dark exciton level further below the bright exciton level and increasing the dark exciton lifetime (τ_D) with increasing

quantum confinement.[8, 46] In weakly confined $FAPbBr_3$ NCs (9.2 nm), a recent study of single-particle PL reported that dark exciton level lies 2.5 meV below bright exciton[44].

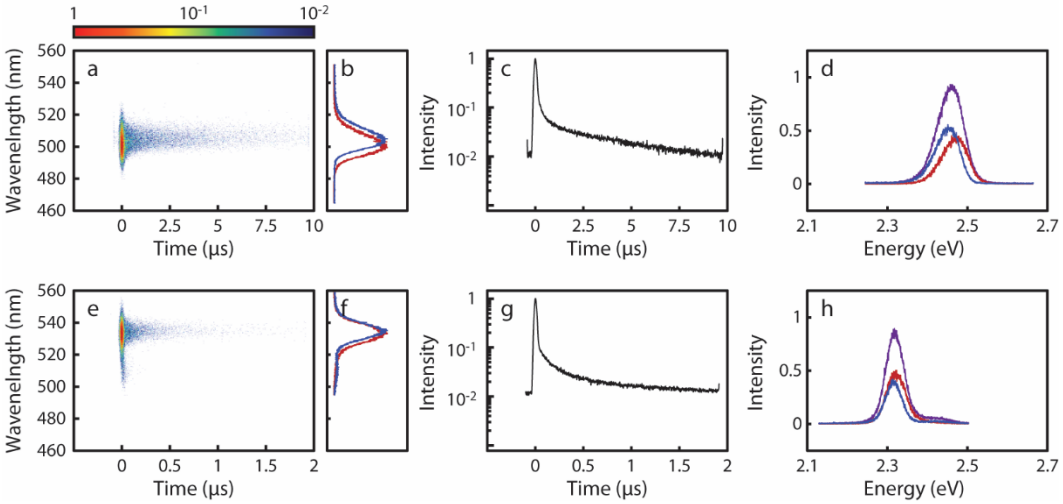

Figure 13(a, e) Time-resolved PL spectra, (b, f) time gated PL spectra at short (red) and long (blue) time windows, (c, g) time-dependent integrated PL intensity, and (d, h) PL spectra decomposed into bright (red) and dark (blue) exciton PL at 5 K for $FAPbBr_3$ QDs of 2 sizes. (a, b, c, d) 3.6 nm, (e, f, g, h) 6.2 nm. Reprinted with permission from Tang, X. et al *J. Phys. Chem. C* **2022**, *126*, 18366-18373. Copyright 2022 American Chemical Society.

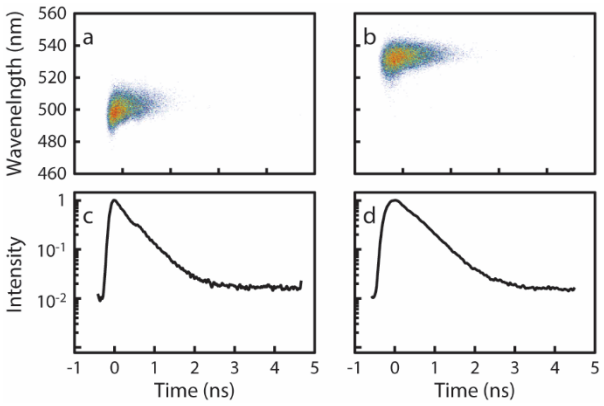

Figure 14 (a, b) Time-resolved PL spectra and (c, d) time-dependent PL intensities of $FAPbBr_3$ QDs of two different sizes measured at 5 K in 5 ns time window: (a, c) 3.6 nm, (b, d) 6.2 nm. Reprinted with permission from Tang, X. et al *J. Phys. Chem. C* **2022**, *126*, 18366-18373. Copyright 2022 American Chemical Society.

To examine whether the quantum confinement has the same effect on the bright-dark level splitting ($\Delta E_{BD} = E_{bright} - E_{dark}$) and τ_D as in $CsPbBr_3$ QDs, we compared the time-dependent PL spectra of $FAPbBr_3$ QDs of different sizes (3.6 and 6.2 nm) at 5K. At this temperature, dark exciton PL distinguishable from bright exciton PL as the μs-decay component is clearly visible in Figure 13a and e. The time-dependent PL intensities of both QDs are shown in Figure 13c and g, where the slow decay component of the PL (time constant: τ_{slow}) attributed to dark exciton is well-separated from the faster decay component (time constant: τ_{fast}) attributed to bright exciton. Magneto-fluorescence data that further supports the slow decay component of the PL to dark exciton will be discussed further below. τ_{slow} was determined from the fitting of the data in Figure 13c and g. τ_{fast} that is in sub-ns time scale was determined from a separate set of time-dependent PL

spectra obtained in several ns time window providing the sufficient time resolution as shown in Figure 14. The sub-ns and μs components of the PL can also be separated spectrally by integrating the time-resolved PL spectra in different time windows. This allows decomposing the PL spectra into the contributions from bright and dark exciton PL as shown in Figure 13b, d, f and h, where the splitting between the two peaks is interpreted as ΔE_{BD}.[8] Table 2 summarizes the peak wavelength for the bright (λ_B) and dark (λ_D) exciton PL, ΔE_{BD} and the two PL decay time constants (τ_{fast} and τ_{slow}) for the $FAPbBr_3$ QDs of the two different sizes.

Table 2 Spectroscopic parameters and lifetimes of exciton PL at 5 K shown in Figure 13. λ_B (E_B) and λ_D (E_D) are the wavelengths (energy) for bright and dark exciton PL, ΔE_{BD} is the bright-dark level splitting ($E_B - E_D$), τ_{fast} and τ_{slow} are the time constants for the fast and slow decay components of the PL respectively. τ_{slow} at 5 K is also interpreted as the dark exciton lifetime (τ_D). Reprinted with permission from Tang, X. et al *J. Phys. Chem. C* **2022**, *126*, 18366-18373. Copyright 2022 American Chemical Society.

QD size	**λ_B (E_B)**	**λ_D (E_D)**	**ΔE_{BD}**	**τ_{fast}**	**τ_{slow} (τ_D)**
3.6 nm	500.5 nm (2.4772 eV)	504.3 nm (2.4586 eV)	18.6 meV	0.39 ns	3.1 μs
6.2 nm	533.4 nm (2.3244 eV)	534.8 nm (2.3184 eV)	6.0 meV	0.53 ns	1.2 μs

It is important to note that ΔE_{BD} in Table 2 is larger for the smaller $FAPbBr_3$ QDs and that ΔE_{BD} values of both QDs are larger than ΔE_{BD} of 2.5 meV reported for 9.2 nm $FAPbBr_3$ NCs in an earlier study.[44] The same trend, i.e., increasing ΔE_{BD} with increasing quantum confinement, was also observed in the strongly confined $CsPbBr_3$ QDs and NPLs.[46, 90] This was explained by the increasing electron-hole exchange energy with decreasing QD volume resulting in the increase of ΔE_{BD}. Therefore, one can conclude that both $FAPbBr_3$ QDs and $CsPbBr_3$ QDs exhibit the same effect of confinement-enhanced exchange energy in their size-dependent ΔE_{BD}. In the larger weakly confined NCs, on the other hand, $CsPbBr_3$ and $FAPbBr_3$ are reported to exhibit the opposite bright and dark exciton level order, i.e., negative ΔE_{BD} for $CsPbBr_3$ and positive ΔE_{BD} $FAPbBr_3$. This was considered due to the difference in the balance between the two opposing contributions, i.e., Rashba effect and exchange interaction, in determining the relative ordering of bright and dark exciton level. However, the enhanced electron-hole exchange interaction by the quantum confinement should be the dominating factor for both $CsPbBr_3$ and $FAPbBr_3$ QDs in strongly confined regime, therefore placing the dark state below the bright state with increasing ΔE_{BD} with increasing confinement[41].

In the exciton level scheme, where the bright state is located above the dark state, we interpret τ_{fast} as the decay time constant for the bright exciton level via the recombination of bright exciton and bright-to-dark transition following the same analysis made for $CsPbBr_3$ QDs in our earlier study.[8] Since 5 K is a sufficiently low temperature to effectively prevent the thermal excitation of the dark state to the bright state, τ_{slow} can be interpreted as the dark exciton lifetime (τ_D). Compared to τ_D of $CsPbBr_3$ QDs of

comparable sizes[8, 46], τ_D of $FAPbBr_3$ QDs are several times smaller, as summarized in Table 3. While the smaller τ_D of $FAPbBr_3$ QDs may be interpreted as the stronger bright-dark level mixing if the nonradiative decay of dark state at 5 K is negligible. However, more extensive temperature-dependent PL spectra and PL quantum yield data as well as further theoretical studies will be required to make a more conclusive interpretation of the shorter τ_D.

Table 3 Bright-dark splitting (ΔE_{BD}) and two PL time constants of $CsPbBr_3$ QDs and $FAPbBr_3$ QDs of the similar sizes. Reprinted with permission from Tang, X. et al *J. Phys. Chem. C* **2022**, *126*, 18366-18373. Copyright 2022 American Chemical Society.

QD	**Size**	**ΔE_{BD}**	**τ_{fast}**	**τ_{slow} (τ_D)**
$CsPbBr_3$	3.9 nm	17meV	0.31 ns	14 μs
	6.5 nm	3.5 meV	N/A	2.5 μs
$FAPbBr_3$	3.6 nm	18.6 meV	0.39 ns	3.1 μs
	6.2 nm	6.0 meV	0.53 ns	1.2 μs

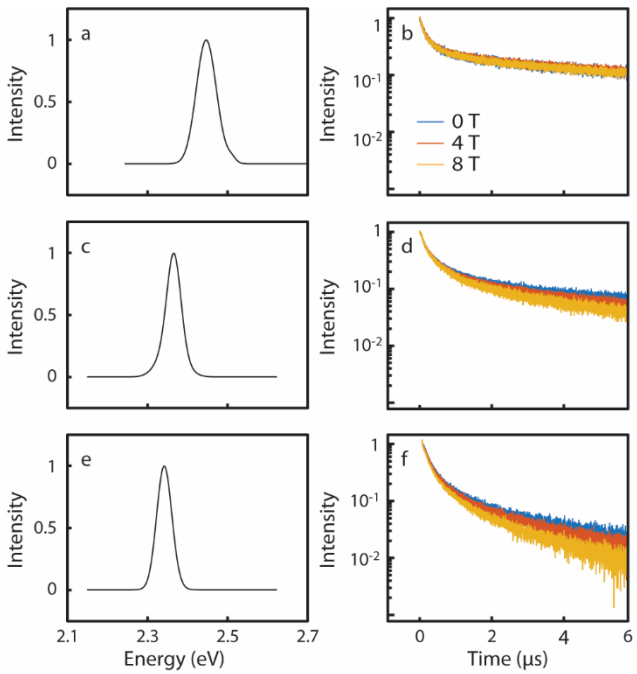

Figure 15 Steady state PL spectra (a, c, e) and magnetic field-dependent PL decay curves (b, d, f) of $FAPbBr_3$ QDs of different sizes measured at 5 K. (a, b) 3.7 nm, (c, d) 5.2 nm and (e, f) 5.7 nm. Reprinted with permission from Tang, X. et al *J. Phys. Chem. C* **2022**, *126*, 18366-18373. Copyright 2022 American Chemical Society.

Since the external magnetic field mixes bright and dark exciton states in MHP NCs, which gives more oscillator strength to the dark exciton and accelerate the relaxation of dark exciton, we examined the effect of external magnetic field on τ_D of $FAPbBr_3$ QDs of varying sizes. Figure 15 shows the time-dependent PL intensities of $FAPbBr_3$ QDs of three different sizes at 5 K at varying external magnetic fields together with the steady state PL spectra at 5 K without external magnetic field. This measurement was performed using a relatively long excitation pulse (405 nm, 150 ns), which does not resolve the fast decay component of bright exciton, therefore only the slow decay component of the PL

was examined as a function of external magnetic field. Table 4 summarizes τ_D at 0, 4 and 8 T of magnetic field. With decreasing size of $FAPbBr_3$ QDs, τ_D becomes less sensitive to the magnetic field, which is consistent with the expectation from the perturbation theory that predicts the stronger mixing of the two states by the perturbation (magnetic field) with the smaller energy gap. It is interesting to see that the smallest $FAPbBr_3$ QDs (3.7 nm) show nearly constant τ_D between 0 and 8 T, whereas $CsPbBr_3$ QDs of similar size showed significantly stronger dependence of τ_D on the magnetic field in the earlier study[8]. The difference in the sensitivity of τ_D to the magnetic field between $CsPbBr_3$ QDs and $FAPbBr_3$ QDs is not clear yet. Whether the asymmetry and the presence of internal nuclear degrees of freedom of the organic cation play a role in this difference will be an interesting question to answer in future studies.

Table 4 Dark exciton PL lifetime of different sized FAPbBr3 QDs at varying external magnetic fields at 5 K. EPL is the PL peak energy. τD,0T, τD,4T and τD,8T are the dark exciton PL lifetime at 0 T, 4 T and 8 T respectively. Reprinted with permission from Tang, X. et al *J. Phys. Chem. C* **2022**, *126*, 18366-18373. Copyright 2022 American Chemical Society.

QD size	**E_{PL}**	**$\tau_{D,0T}$**	**$\tau_{D,4T}$**	**$\tau_{D,8T}$**
3.7 nm	2.4498 eV	2.8 μs	2.8 μs	2.8 μs
5.2 nm	2.3684 eV	2.2 μs	2.1 μs	1.9 μs
5.7 nm	2.3451 eV	1.9 μs	1.6 μs	1.2 μs

3.4. **Conclusion**

We synthesized strongly quantum-confined $FAPbBr_3$ QDs and investigated the effect of quantum confinement on the exciton PL properties and exciton fine structure. The strongly quantum-confined $FAPbBr_3$ QDs show an increasing bandgap with decreasing QD size, which is comparable in the magnitude to that of $CsPbBr_3$ QDs in the similar size range. PL of $FAPbBr_3$ QDs show a redshift and linewidth narrowing with decreasing temperature in 78 - 295 K range, which is also qualitatively similar to the behavior of $CsPbBr_3$ QDs. Time-resolved PL spectra of $FAPbBr_3$ QDs at 5 K revealed intense PL from dark lowest-energy exciton state with μs lifetime. The bright-dark level splitting (ΔE_{BD}) increased with increasing quantum confinement, consistent with the expectation from the confinement-enhanced electron-hole exchange energy that increases ΔE_{BD}, which is also in line with the observation made in $CsPbBr_3$ QDs. On the other hand, the dark exciton lifetime (τ_D) was significantly shorter than that of the comparably sized $CsPbBr_3$ QDs possibly suggesting the stronger mixing of bright and dark state. Under the external magnetic field, τ_D decreased at the higher field with decreasing sensitivity of τ_D to the magnetic field with decreasing QD size. When compared to $CsPbBr_3$ QDs of the same size, shortening of τ_D via magnetic mixing is less in $FAPbBr_3$ QDs, although whether the organic cation plays a role in this difference is uncertain.

4. CHAPTER IV

EFFECTS OF ELECTRONIC COUPLING ON BRIGHT AND DARK EXCITONS IN 2-DIMENSIONAL ARRAY OF STRONGLY CONFINED $CsPbBr_3$ QUANTUM DOTS*

4.1. Introduction

Exciton properties of non-interacting colloidal quantum dots (QDs) of a given material are dictated by the spatial distribution and electronic interactions of electron and hole dependent on the size, shape, surface ligands and surrounding medium of the QDs. When the QDs are sufficiently close to each other, overlap of exciton wavefunctions or increased dipolar interaction between the QDs can alter the exciton level structure and dynamics via electronic coupling or interparticle energy/charge transfer.[69, 71, 91, 92] These result in the photophysical properties of interacting ensemble of QDs different from the isolated QDs, such as redshift of the exciton transition energy[69, 93-96] and increased electrical conductivity[97-101] observed in densely packed film of QDs. To bring the QDs sufficiently close to increase the interparticle interaction, often, 2-dimensional (2D) and 3-dimensional (3D) arrays of QDs were created after replacing the long-chain organic ligands typically used to passivate the surface of the QDs with shorter ones.[99, 101, 102] In some cases, directly connected QD dimers were created to introduce electronic coupling between the QDs that gives rise to the properties of two coupled excitons.[71, 103, 104]

---

* Reprinted with permission from Tang, X.; Rossi, D.; Cheon, J.; Son, D. H. Effects of Electronic Coupling on Bright and Dark Excitons in a 2D Array of Strongly Confined $CsPbBr_3$ Quantum Dots. *Chem. Mater.* **2022**, *34*, 7181-7189. Copyright 2022 American Chemical Society.

Earlier studies on the properties of 2D and 3D array of QDs were performed mostly with II-VI and IV-VI QDs with the focus on enhancing their properties for light-emitting and photovoltaic applications.[91, 105] More recently, the interest in the role of electronic or dipolar coupling in the QD arrays expanded into lead halide perovskite (LHP) nanocrystals (NCs) that emerged as a superior alternative to many existing semiconductor QDs in these applications.[6, 63] Several recent studies in 3D superlattices of LHP NCs reported the observation of superfluorescence and change in incoherent exciton emission propagating through the superlattice.[106-111] However, most of these studies on the array of LHP NCs were performed with weakly or non-confined NCs passivated with long-chain ligands, therefore interparticle interaction was relatively weak in these systems. Recent synthetic progress enabled the production of strongly quantum confined LHP QDs with high uniformity previously difficult to obtain[19], which also exhibit quite different exciton properties from that of weakly or non-confined counterparts. For instance, strongly quantum confined $CsPbX_3$ QDs exhibited intense and μs-lived photoluminescence (PL) from dark exciton at low temperatures, in contrast to weakly confined QDs whose PL is dominated by bright exciton[8]. Therefore, strong confinement in LHP QDs not only facilitates the interparticle electronic coupling via increased wavefunction overlap, but also gives access to dark exciton that may function as the source of photon, charge or quantum information carrier that can benefit from its longevity.

To this end, we created well-ordered 2D arrays of strongly quantum confined $CsPbBr_3$ QDs with facet-to-facet distance of several angstroms (Å) and investigated the effect of electronic coupling on the energetics and dynamics of bright and dark exciton.

For this purpose, we employed a ligand exchange method replacing the surface-bound long-chain organic ligand with NaBr, which can create the 2D arrays of QDs with the facet-to-facet distance reduced to ~5 Å.[29] From the spectrally and temporally resolved measurement of the PL at varying temperatures (5-300K), we investigated how the electronic coupling alters the level structure and relaxation dynamics of bright and dark exciton in strongly confined $CsPbBr_3$ QDs. Results from the present study will be important in utilizing electronically coupled LHP QDs in the strongly confined regime, in which both bright and dark excitons are accessible as the source of photons or charges.

4.2. Experimental Section

4.2.1. Synthesis of $CsPbBr_3$ QDs.

Strongly quantum confined $CsPbBr_3$ QDs were synthesized employing the previously published procedure[19] briefly described below. The Cs precursor was prepared by dissolving Cs_2CO_3 (0.25 g) in the mixture of oleic acid (OA, 0.8 g) and 1-octadecene (ODE, 7 g) at 130 °C under N_2 atmosphere on a Schlenk line after degassing at room temperature for 10 minutes under vacuum. The Pb/Br precursor was prepared by dissolving $PbBr_2$ (190 mg) and $ZnBr_2$ (500 mg) in the mixture of ODE (6 mL), OA (3.2 mL) and Oleyl amine (OAm, 3.2 mL) and heating at 120 °C under vacuum for 5 min. The reaction was initiated by injecting 2 mL of Cs precursor solution into Pb/Br precursor solution under N_2 atmosphere at a chosen reaction temperature to obtain the QDs of different sizes. (80 °C for 3.8 nm QDs, 120 °C for 4.2 nm QDs and 160 °C for 5.3 nm QDs). After ~3 minutes of reaction, the product was cooled down to room temperature.

After letting the remaining excess reactant to precipitate at room temperature, QDs were recovered from the supernatant after centrifuging the product mixture. The removal of remaining excess reactant via precipitation from the supernatant containing QDs were repeated several times. The recovered QDs were purified by precipitating with acetone and redispersing in hexane.

4.2.2. Ligand Replacement from oleylammonium bromide (OLAB) to NaBr.

The ligand replacement from OLAB to NaBr was performed using the procedure modified from the previously published method, which involves sequential two-step exchange.[29] Two ligand precursor solutions were prepared for this purpose: phenylethyl ammonium bromide (PEAB, 250 mg) in 1 mL anhydrous Dimethylformamide (DMF) and NaBr (100 mg) in 1 mL anhydrous DMF. Initially, concentrated OLAB-passivated QD solution in hexane (300 μL, 0.8 mM) was precipitated with methyl acetate and redispersed in toluene three times, which partially removed the OLAB ligand, resulting in a loss of the PL intensity. Subsequently, 10 μL of PEAB solution in DMF was added to the QD solution and mixed vigorously. After removing the precipitated excess PEAB salt by centrifuging, addition of PEAB solution and removal of excess PEAB were repeated 3 more times. At this stage, the QD solution recovered PL intensity almost to the initial level. After precipitation with methyl acetate and dispersion of the PEAB-treated QDs in toluene, 5 μL of NaBr solution in DMF was added to the QD solution and mixed vigorously. The excess NaBr salt was removed in the same manner as PEAB. After repeating the addition of NaBr solution and removal of excess NaBr, the final NaBr-passivated QDs were recovered by precipitation with methyl acetate and redispersed in toluene.

4.2.3. Preparation of 2D Close-Packed Arrays of QD.

The 2D close-packed arrays of the QDs were formed directly on a TEM grid for both TEM imaging and spectroscopic measurements. The concentration of the QD solutions to prepare the array sample was adjusted to have absorbance of ~30 at 400 nm for 1 cm pathlength. 25 μL of QD solution in the mixture of toluene and hexane was drop-casted on a carbon supported copper TEM grid and left under ambient condition for 5 minutes for the solvent to evaporate. TEM images of the close-packed 2D arrays of the QDs were acquired using the FEI Tecnai G2 F20 ST FE-TEM at 200 kV.

4.2.4. Optical Measurements.

Steady state absorption and PL spectra of the solution QD samples were obtained with Ocean Optics USB spectrometer (USB2000, QE65). The PL spectra of the 2D arrays of QDs on the TEM grid under ambient condition were obtained with a CCD camera (Princeton Instruments, ProEM+) and an imaging spectrograph (Princeton Instruments, Acton SpectraPro SP-2300) under excitation at 390 nm. Temperature-dependent steady state and time-resolved PL spectra of the 2D arrays of QDs on the TEM grids were obtained using an open-cycle cryostat (Oxford Instruments Microstat-HE) in conjunction with a home-built microscope. The samples were excited with a 405 nm pulsed diode laser (Horiba, 45 ps pulse width). Steady state PL spectra of the samples in the cryostat were obtained using a CCD camera (Andor, iXon) coupled to an imaging spectrograph (Andor, Kymera 328i) except the data in Fig. 4e. PL spectra in Fig. 4e were obtained using a combination of a different spectrograph (Princeton Instruments, Acton MicroSpec 2150i) and CCD (Princeton Instruments, PIXIS 100) using another open-cycle cryostat (Janis ST-

500). Time-resolved PL intensities of the arrays of 4.2 nm QDs (Fig. S9) at 5 K were obtained using a 405 nm, 150 ns pulsed LED as the excitation source and time-correlated single photon counting (PicoHarp 300) with an avalanche photodiode (MPD PDM series) for detection.

4.3. Results and Discussion

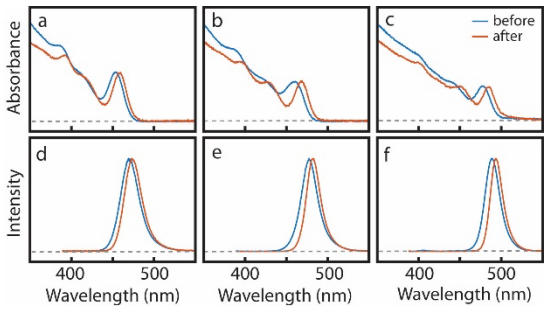

Figure 16 Solution-phase absorption (a-c) and PL (d-f) spectra of $CsPbBr_3$ QDs before (blue) and after (red) the ligand exchange from OLAB to NaBr. The size of the QDs after the ligand exchange determined from the size-dependent exciton PL peak is (a, d) 3.8 nm, (b, e) 4.2 nm, (c, f) 5.3 nm. Reprinted with permission from Tang, X. et al. *Chem. Mater.* **2022**, *34*, 7181-7189. Copyright 2022 American Chemical Society.

To investigate the effect of electronic coupling on the PL of bright and dark exciton in strongly quantum confined $CsPbBr_3$ QDs, the original surface ligand (OLAB) was replaced with NaBr following the recently reported procedure[29] as detailed in the Experimental Section. This replacement was necessary to reduce the facet-to-facet distance of the QDs of cube morphology from ~3 nm to sub-nm regime, allowing for the overlap of the exciton wavefunction. Figure 16 shows the absorption and emission spectra

of $CsPbBr_3$ QDs of several different sizes in the strongly confined regime dispersed in hexane before and after the ligand replacement from OLAB to NaBr. A small redshift of the exciton peaks and narrowing of their linewidth are observed after the ligand exchange for the QDs of all sizes. However, this is considered mainly from the additional size selection or/and minor surface reconstruction during the ligand exchange and purification process rather than the intrinsic effects of putting different ligand on the QD surface. This is because NaBr should not spatially expand the electron or hole wavefunctions, in contrast to some organic ligands known to spatially delocalize the wavefunction resulting in the redshift of the exciton transition.[112]

The negligible difference of the effects of OLAB and NaBr on the PL spectra was further confirmed by comparing the PL spectra of the $CsPbBr_3$ QDs ligand-exchanged with NaBr and OLAB using the same batch of the ligand-stripped QDs. The evolution of the PL spectra at each stage of the ligand exchange process are shown in Figure 17. In this work, we used the pairs of OLAB- and NaBr-passivated QDs with closely matching exciton PL spectra, which are chosen from multiple batches of QD samples rather than directly comparing the samples shown in Figure 16, for the study of the effects of electronic coupling.

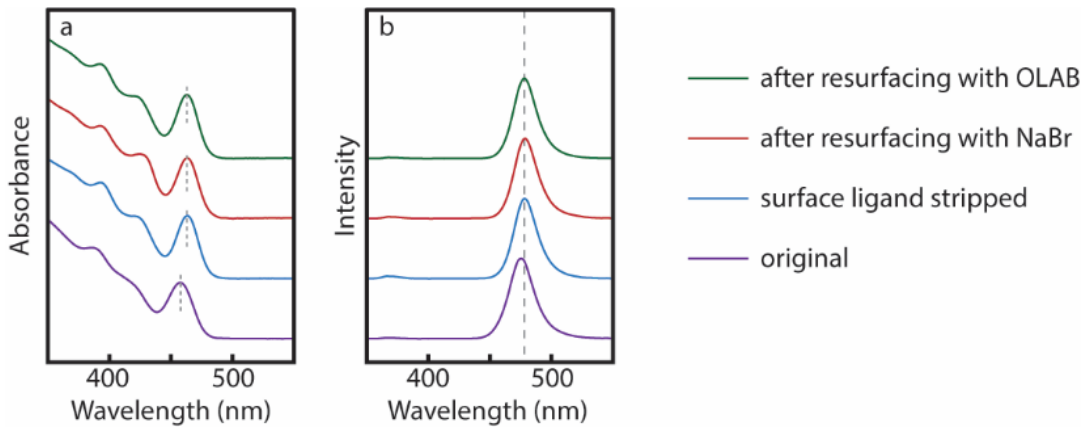

Figure 17 Absorption (a) and photoluminescence (PL, b) spectra of the QDs during the process of ligand exchange. Purple: As-synthesized QDs passivated with OLAB, Blue: Partially ligand-stripped QDs recovered after the centrifugation and resuspension in solvent, Red: QDs re-passivated with NaBr, Green: QDs re-passivated with OLAB. Reprinted with permission from Tang, X. et al. *Chem. Mater.* **2022**, *34*, 7181-7189. Copyright 2022 American Chemical Society.

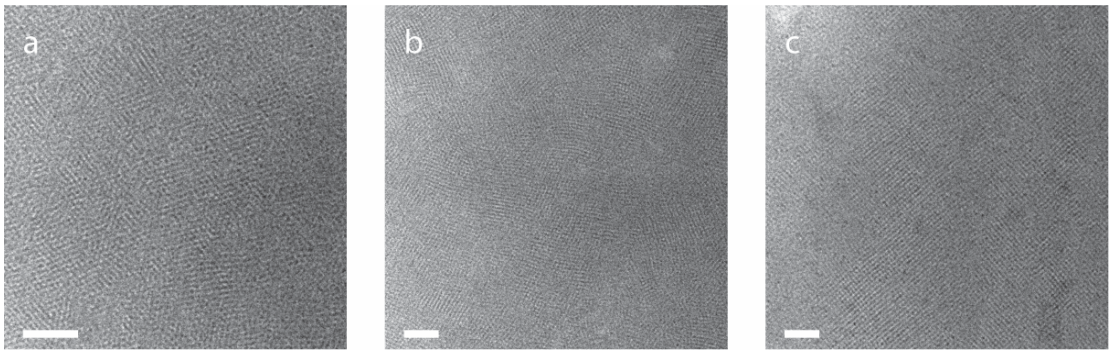

Figure 18 TEM images of the ordered arrays of $CsPbBr_3$ QDs passivated with NaBr (a: 3.8 nm, b: 4.2 nm, c: 5.3 nm) formed on the TEM grid at a lower magnification. (Scale bar: 50 nm). Reprinted with permission from Tang, X. et al. *Chem. Mater.* **2022**, *34*, 7181-7189. Copyright 2022 American Chemical Society.

As shown in Figure 18, survey of large area on the TEM grid indicates that 2D close-packing of the QDs occur on the length scale of several hundred nm or larger, while grain boundaries are observed. Figure 19 shows the higher magnification TEM images of OLAB- and NaBr-passivated QDs for three different sizes in strongly confined regime and PL spectra of the close-packed arrays of these QDs at room temperature. TEM images show well-ordered arrays of both OLAB- and NaBr-passivated QDs.

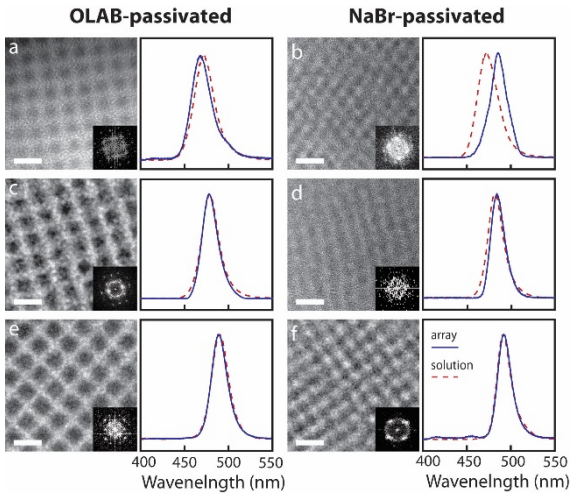

Figure 19 TEM images and room-temperature PL spectra of the 2D arrays of $CsPbBr_3$ QDs passivated with OLAB (a,c,e) and NaBr (b,d,f) formed on the TEM grids. PL spectra of the QD solution samples (dashed) are also shown for comparison. Size of the QDs and PL peak position are in Table 5. Inset in each TEM image is Fourier transform of the image. Scale bar is 10 nm. Reprinted with permission from Tang, X. et al. *Chem. Mater.* **2022**, *34*, 7181-7189. Copyright 2022 American Chemical Society.

The PL spectra were taken under ambient condition directly from the TEM grids where the close-packed arrays of QDs are formed on an optical microscope following the weak *cw* excitation at 390 nm. The area on the TEM grid where the PL was measured is approximately 4×4 μm^2, which would contain multiple islands of 2D arrays of QDs. As a reference for the comparison, the solution-phase PL spectra of the corresponding QD samples dispersed in hexane are also shown (dashed curve).

Table 5 Center-to-center distance ($d_{c\text{-}c}$) between the QDs of edge length (l) formed on the TEM grid, PL peak wavelengths of the QD arrays (λ_{array}) and QD solution samples (λ_{sol}), and PL peak redshift in the QD array referenced to the solution sample (ΔPL) shown in Figure 19. Reprinted with permission from Tang, X. et al. *Chem. Mater.* **2022**, *34*, 7181-7189. Copyright 2022 American Chemical Society.

Sample	Ligand	l	$d_{c\text{-}c}$	λ_{sol}	λ_{array}	ΔPL
a	OLAB	3.8 nm	6.8 nm	471.9 nm	468.1 nm	-21 meV
b	NaBr		4.5 nm	472.0 nm	485.6 nm	74 meV
c	OLAB	4.2 nm	7.4 nm	478.6 nm	478.2 nm	-2 meV
d	NaBr		4.9 nm	481.8 nm	484.2 nm	13 meV
e	OLAB	5.3 nm	7.9 nm	490.2 nm	489.0 nm	-6 meV
f	NaBr		5.8 nm	491.2 nm	492.1 nm	4 meV

Table 5 summarizes the PL peak positions from the QD solution samples and the arrays of QDs formed on the TEM grid. Center-to-center distances ($d_{c\text{-}c}$) of both OLAB- and NaBr-passivated QDs determined from the TEM images and their Fourier transform are also compared. For all three different sizes, $d_{c\text{-}c}$ decreases by 2.1-2.5 nm when OLAB is replaced with NaBr, resulting in a facet-to-facet distance of ~5Å in the array of NaBr-passivated QDs. While thermal annealing of the close-packed QD arrays generally makes the QDs closer, as has been evidenced by increased electrical conductivity in the earlier studies,[95, 97] thermal annealing was avoided in this study to minimize merging of the QDs and possible additional structural changes during heating.

The OLAB-passivated QDs show very similar PL spectra between the solution sample and QD arrays on TEM grid, although a small blueshift is noticeable for the smallest QDs (l=3.8 nm) whereas the larger QDs show essentially identical PL spectra. In contrast, 2D arrays of NaBr-passivated QDs show increasing redshift compared to the solution sample with decreasing size of the QDs. The smallest NaBr-passivated QDs (l=3.8 nm) exhibit particularly large redshift of the PL (74 meV) in close-packed array with respect to the solution phase, which is much larger than 13 and 4 meV redshift observed in the QDs with l=4.2 and 5.3 nm respectively. When compared to the close-packed array of OLAB-passivated QDs, the redshift exhibited by l=3.8 nm QDs increases to 95 meV. The possibility of the change in dielectric environment as the cause for the large PL peak redshift of QDs in the arrays was ruled out. The PL spectra of 3.8 nm QDs

in solvents with varying dielectric constants in the range of ε=1.9-5.6 (ε for $CsPbBr_3$ = 7.3) showed much smaller PL redshift of less than 19 meV, as shown by Figure 20.

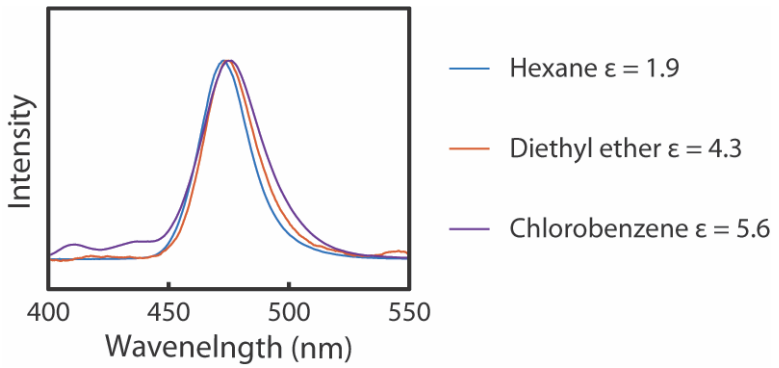

Figure 20 PL spectra of 3.8 nm OLAB-passivated QDs dispersed in solvents of different dielectric constant (e). Peak positions are 472.5 nm (hexane), 474.6 nm (diethyl ether) and 476.0 nm (chlorobenzene). The difference of peak energies in hexane and chlorobenzene 19 meV. Reprinted with permission from Tang, X. et al. *Chem. Mater.* **2022**, *34*, 7181-7189. Copyright 2022 American Chemical Society.

Typically, the redshift of PL in the close-packed array of colloidal QDs has been explained by either the electronic coupling between the adjacent QDs or (and) energy transfer between the energetically heterogeneous ensemble of the QDs. Both electronic coupling and energy transfer become more efficient with decreasing interparticle distance qualitatively consistent with our observation. However, the redshift of the PL in the array of NaBr-passivated QDs in our study is largely attributed to the electronic coupling facilitated by short facet-to-facet distance and strong quantum confinement as will be discussed further below. Since the smallest QDs (l=3.8 nm) exhibit the largest redshift of the PL in the close-packed array, our discussion about the effect of electronic coupling on

the bright and dark excitons in $CsPbBr_3$ QDs will focus more on l=3.8 nm QDs, which will be compared with the larger QDs (l=4.2 nm) that exhibit much weaker effect. It is worth noting that redshift of the PL in the array of l=3.8 nm NaBr-passivated QDs is also sensitive to the degree of order in the QD array,[113] showing smaller PL redshift with more disorder in the QD array, as shown in Figure 21. For the array of l=3.8 nm NaBr-passivated QDs showing regular ordered arrangement on the TEM image, the PL peak shift with respect to solution PL (ΔPL) varied in 45-74 meV range depending on the batches of QD used to form the arrays that may result from small variation of the order or $d_{c\text{-}c}$.

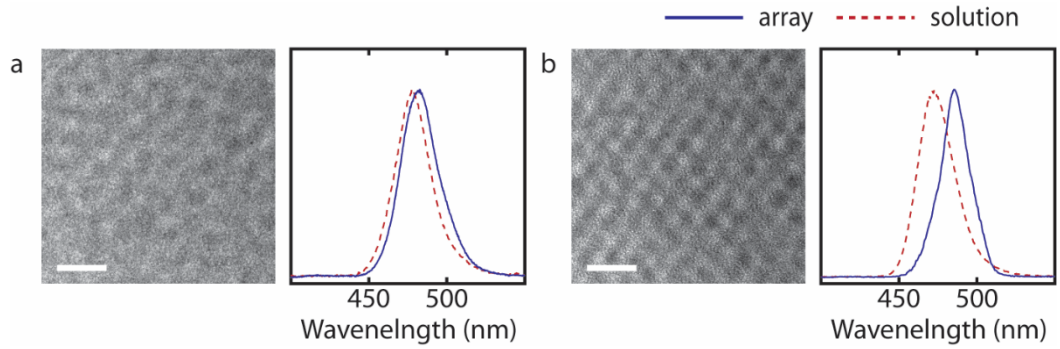

Figure 21 TEM images and room-temperature PL spectra of less ordered array of 3.8 nm $CsPbBr_3$ QDs passivated with NaBr formed on the TEM grid (a), showing less PL redshift (24 meV) compared to more ordered array (b, same as in Figure 19b). Reprinted with permission from Tang, X. et al. *Chem. Mater.* **2022**, *34*, 7181-7189. Copyright 2022 American Chemical Society.

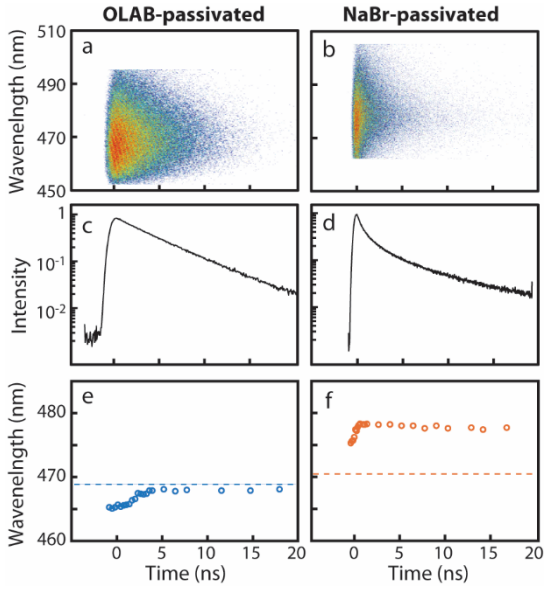

Figure 22 (a,b) Time-dependent PL spectra, (c,d) time-dependent PL intensity and (e,f) time-dependent PL peak position of the array of $CsPbBr_3$ QDs (l=3.8 nm) passivated with OLAB (a,c,e) and NaBr (b,d,f) at 300 K. Horizontal lines in panel e and f are the PL peak position in solution. Reprinted with permission from Tang, X. et al. *Chem. Mater.* **2022**, *34*, 7181-7189. Copyright 2022 American Chemical Society.

One of the unique properties of exciton of the strongly quantum confined $CsPbBr_3$ QDs compared to weakly and non-confined counterparts is the accessibility to the lowest-energy dark exciton level that exhibits intense and long-lived dark exciton PL[8]. Our recent studies in strongly confined $CsPbBr_3$ and $CsPbI_3$ QDs showed that increasing quantum confinement results in the larger bright-dark energy splitting (ΔE_{BD}) and increasing dark exciton lifetime, which makes the dark exciton more readily accessible at the higher temperatures.[46] To confirm the electronic coupling as the main cause for the PL redshift in the array of NaBr-passivated QDs and its effect on exciton fine structure, specifically

on the relative energetics and dynamics of bright and dark exciton, steady state and time-dependent PL spectra at varying temperatures in 5-300 K range were obtained for l=3.8 nm QDs. The PL spectra from the array of OLAB-passivated QDs of the same size were also obtained as the reference for the comparison, in which the electronic coupling between the QDs is negligible.

First, we examine the dynamic PL spectra at 300 K, at which bright exciton dominates the PL emission, using the QD arrays on TEM grid placed in a vacuum cryostat. 405 nm pulsed light (45 ps, 1kHz) was used to excite the sample at sufficiently low fluence (50 nJ/cm^2) to ensures very low excitation density (~5×10^{-4} exciton/QD based on the reported absorption cross section of ~4.5×10^{-15} cm^2).[114] For the detection of the time-dependent PL, a streak camera was used. Figure 22 shows the time-dependent PL spectra (a, b), time-dependent PL intensities (c, d), and time-dependent PL peak positions (e, f) of the arrays of OLAB- and NaBr-passivated QDs at 300 K. In solution phase, these OLAB- and NaBr-passivated QDs exhibited similar PL peak at 468.4 nm and 470.4 nm, respectively as indicated by the dashed line in Figure 22e and f. The linewidth of the solution-phase PL spectra is ~150 meV for both samples indicating the similar ensemble heterogeneity. Note that the batch of the array of NaBr-passivated QDs for the temperature-dependent measurement in cryostat is different from that of Figure 19b measured under ambient condition, and ΔPL is smaller (45 meV) because of the batch-to-batch variation as mentioned earlier.

The array of OLAB-passivated QDs exhibit almost single-exponential PL decay with the time constant of τ=4.2 ns, which is close to that of solution sample (τ=4~5 ns).[115]

On the other hand, the array of NaBr-passivated QDs exhibits multiexponential decay, which exhibits a sub-ns decay component (τ=0.42 ns) that is absent in solution PL and a slower decay component with average time constant of τ=8.8 ns. Earlier studies in the QD solids and chemically linked or directly bound QD dimer also observed the appearance of fast-decaying PL absent in solution PL.[71, 103, 116, 117] This was explained as either energy transfer or charge transfer, which may be possible in our sample too. It is interesting to note that the slower decay time (8.8 ns) of the array of NaBr-passivated QDs that accounts for the majority of photon emission is slower than that of solution sample (3~4 ns). We attribute this to the delocalization of electron and hole wavefunction to a larger volume through the electronic coupling that slows down the radiative recombination.

In Figure 22e and f, both OLAB- and NaBr-passivated QDs show a small dynamic redshift (~2.5 nm) during the early phase of the PL decay, which is absent in the PL from a dilute dispersion of QDs in polystyrene matrix showed in Figure 23.

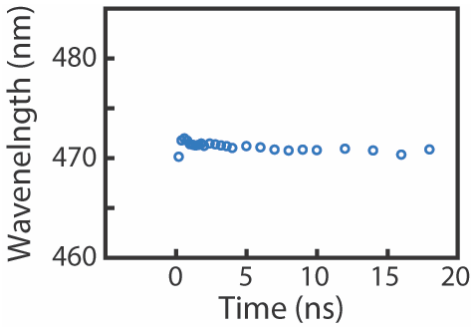

Figure 23 Time dependent PL peak wavelength of QDs dispersed in polystyrene matrix. Reprinted with permission from Tang, X. et al. *Chem. Mater.* **2022**, *34*, 7181-7189. Copyright 2022 American Chemical Society.

It is notable that the dynamic redshift occurs on different time scales in two QD samples; on ~4 ns and sub-ns time scales for OLAB- and NaBr-passivated QDs respectively. The dynamic redshift in the array of OLAB-passivated QDs can be interpreted as the energy transfer between the nearby QDs since such shift is absent in the dilute polymer dispersion of the QDs. The faster sub-ns dynamic redshift in the array of NaBr-passivated QDs may also reflect the energy transfer between the QDs that are more closely spaced than in the array of OLAB-passivated QDs. In this interpretation, the same amount of dynamic redshift is consistent with the similar fwhm of the solution-phase PL at 300 K. While the relaxation within the manifold of the coupled states may be an alternative interpretation, the observed sub-ns time scale of the redshift is much longer than typical relaxation in electronic manifold coupled to phonon degrees of freedom (e.g., ps).

Figure 24a shows the overview of the temperature-dependent steady state PL spectra of the arrays of OLAB- and NaBr-passivated l=3.8 nm QDs. A separate spectrometer operating in conjunction with a streak camera was used for the steady state PL measurement, which provides a higher spectral resolution. With decreasing temperature, both OLAB- and NaBr-passivated QD arrays showed redshift of the PL similar to the previous reports on temperature-dependent PL of $CsPbBr_3$ QDs in solution phase.[9, 50] Temperature-dependent PL peak shift is shown in Figure 24b.

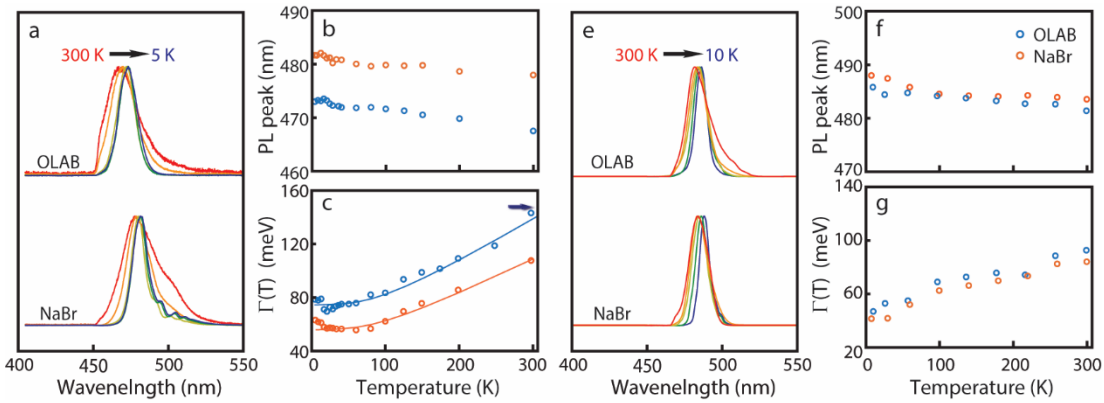

Figure 24(a) Temperature-dependent PL spectra of $CsPbBr_3$ QDs (l=3.8 nm) passivated with OLAB (top) and NaBr (bottom) ligands. The temperatures are 300, 200, 150, 40, 5 K from left to right. Part of the top spectra is cut by a 450 nm long pass filter. (b) Temperature-dependent PL peak wavelength of OLAB- and NaBr-passivated QDs (l=3.8 nm). (c) Temperature-dependent full width at half maximum, Γ(T), of OLAB- and NaBr-passivated QDs (l=3.8 nm). The solid curves are fit to Γ(T) discussed in the text. The arrow indicates Γ(300 K) of the solution-phase PL for both QDs. (e) Temperature-dependent PL spectra of $CsPbBr_3$ QDs (l=4.2 nm) passivated with OLAB (top) and NaBr (bottom) ligands. The temperatures are 300, 180, 100, 60, 10 K from left to right. (f) Temperature-dependent PL peak wavelength of OLAB- and NaBr-passivated QDs (l=4.2 nm). (g) Temperature-dependent Γ(T) of OLAB- and NaBr-passivated QDs (l=4.2 nm). Reprinted with permission from Tang, X. et al. *Chem. Mater.* **2022**, *34*, 7181-7189. Copyright 2022 American Chemical Society.

The broad shoulder near 500 nm in the PL spectrum of the array of NaBr-passivated QDs at 300 K in Figure 24a, which is absent in the array of OLAB-passivated

QDs, is tentatively assigned to the merged QDs existing in the array.[118, 119] This feature becomes more distinct and reveals multiple peaks below 100 K, suggesting that there are several distinct merged QD species with larger effective size, experiencing weaker quantum confinement. The three distinct side peaks in 5 K spectrum of NaBr-passivated QD array in Figure 24a are redshifted by 70, 120 and 145 meV with respect to the main peak at 481.3 nm in Figure 25.

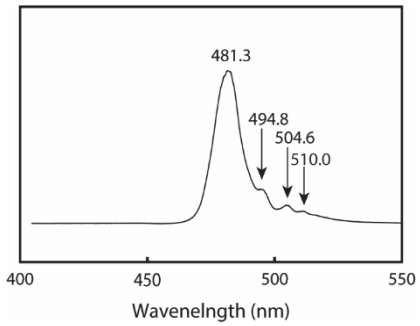

Figure 25 PL spectra of the array of 3.8 nm NaBr-passivated QDs at 5 K. Side peaks on the right side of the main peaks are assigned to the merged QDs. Reprinted with permission from Tang, X. et al. *Chem. Mater.* **2022**, *34*, 7181-7189. Copyright 2022 American Chemical Society.

They do not appear in the 5 K spectra of the arrays of 4.2 nm QDs passivated with either OLAB or NaBr shown in Figure 24e. This excludes the possibility of phonon replica, which should exist in the QD arrays of all sizes and regardless of the ligand[120]. The side peaks occurred only when NaBr-passivated QDs are made into the close-packed arrays, which contrasts with the highly robust PL of the aged QDs in solution phase that

exhibit negligible change over the period of 1 year, as shown in Figure 26, further supporting the merging scenario.

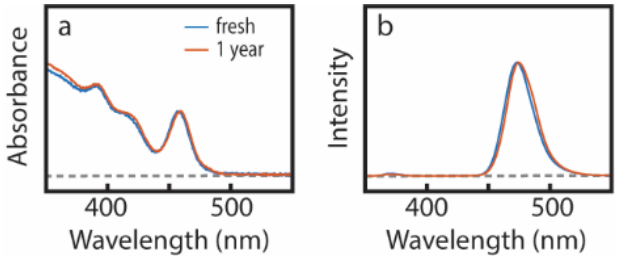

Figure 26 Absorption (a) and PL (b) spectra of the QDs passivated with NaBr that are freshly made and stored in solution at 4°C for 1 year. Reprinted with permission from Tang, X. et al. *Chem. Mater.* **2022**, *34*, 7181-7189. Copyright 2022 American Chemical Society.

In Figure 24c comparing the temperature-dependent full width at half maximum of the PL spectra, Γ(T), the contribution from the shoulder peaks was removed in the PL spectra of the array of NaBr-passivated QDs. Interestingly, the array of NaBr-passivated QDs show the significantly smaller Γ(T) than OLAB-passivated QDs by 20-40 meV in the entire range of temperatures, in contrast to the solution PL spectra at 300 K showing similar Γ(300 K) of ~150 meV for both QDs.

In general, the decreasing PL linewidth would indicate the weakening electron-phonon coupling for the non-interacting ensemble of QDs of a given static inhomogeneity. Γ(T) is often analyzed using a model that includes the contributions from static inhomogeneity (Γ_{inh}) and coupling with acoustic phonon ($\gamma_{ac}T$) and longitudinal

optical (LO) phonon ($\gamma_{LO}N_{LO}$), $\Gamma(T) = \gamma_{LO}N_{LO} + \gamma_{ac}T + \Gamma_{inh}$.[36] γ_{ac} and γ_{LO} represent the coupling strength to acoustic phonon and LO phonon respectively. N_{LO} is the number of the LO phonon mode expressed $N_{LO} = 1/(exp(E_{LO}/k_BT) - 1)$, where E_{LO} is LO phonon energy and k_B is Boltzmann's constant. Fitting the data in Figure 24c to $\Gamma(T)$ described above indicates that γ_{LO} of NaBr-passivated QDs is significantly smaller than that of OLAB-passivated QDs (67 meV vs 86 meV) assuming the same γ_{ac} for both samples, as shown in Figure 27 and Table 6.

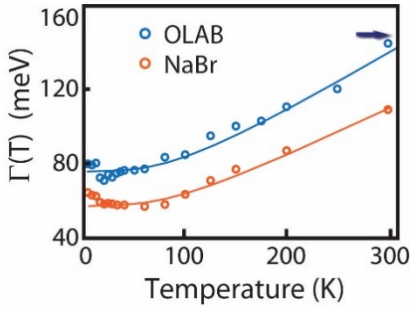

Figure 27 Temperature-dependent full width at half maximum, $\Gamma(T)$, of the PL for the arrays of OLAB- and NaBr-passivated QDs. Solid curves are fit to a model $\Gamma(T) = \gamma_{LO}N_{LO} + \gamma_{ac}T + \Gamma_{inh}$. γ_{ac} and γ_{LO} represent the coupling strength to acoustic phonon and LO phonon respectively. N_{LO} is the number of the LO phonon mode expressed $N_{LO} = 1/(exp(E_{LO}/k_BT) - 1)$, where E_{LO} is LO phonon energy and k_B is Boltzmann's constant. For this fit, the values of γ_{ac} and E_{LO} were kept the same as in Reference 9. The fitting parameters are in Table 6. Reprinted with permission from Tang, X. et al. *Chem. Mater.* **2022**, *34*, 7181-7189. Copyright 2022 American Chemical Society.

Table 6 Best fit parameters of the experimental $\Gamma(T)$ to $\Gamma(T) = \gamma_{LO} N_{LO} + \gamma_{ac} T + \Gamma_{inh}$. Reprinted with permission from Tang, X. et al. *Chem. Mater.* **2022**, *34*, 7181-7189. Copyright 2022 American Chemical Society.

Ligand	γ_{LO}	γ_{ac}	Γ_{inh}	E_{LO}
OLAB	86 meV	20 μeV/K	76 meV	23 meV
NaBr	67 meV	20 μeV/K	57 meV	23 meV

This indicates that the effect of electronic coupling in the 2D array of the QDs is phenomenologically equivalent to reducing the electron-phonon coupling when compared to the uncoupled QDs. While further study is needed to gain a more microscopic understanding of the narrowing of *Γ(T)*, we also note the similarity to the coupled molecular systems such as *J* aggregates that exhibit the narrowing of the absorption linewidth or narrowing of PL linewidth via superradiant emission.[121, 122] In contrast to *l*=3.8 nm QDs, *l*=4.2 nm QDs that exhibit much weaker sign of electronic coupling from their PL spectra show much smaller difference in both PL peak position and Γ(T) between the arrays of OLAB- and NaBr-passivated QDs as shown in Figure 24e-g. This indicates that narrowing of Γ(T) observed in *l*=3.8 nm QDs in Figure 24c is clearly correlates with the electronic coupling.

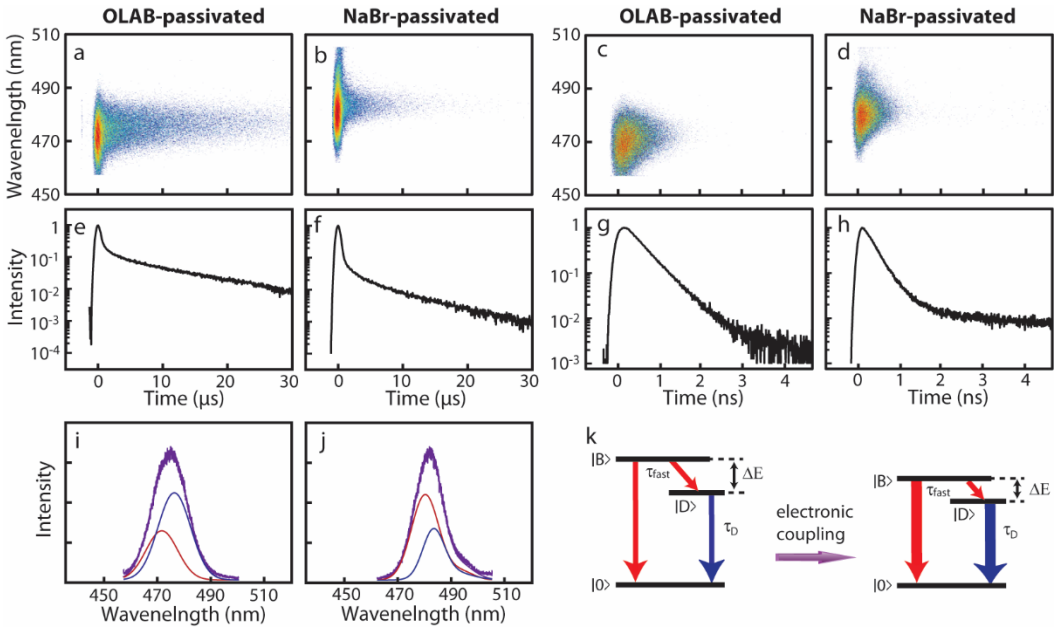

Figure 28 (a-d) Time-dependent PL spectra of the arrays of l=3.8 nm $CsPbBr_3$ QDs passivated with OLAB (a,c) and NaBr (b,d) at 5 K in two different time windows. (e-h) Time-dependent PL intensities of the arrays of l=3.8 nm $CsPbBr_3$ QDs passivated with OLAB (e,g) and NaBr (f,h) at 5 K in two different time windows. (i,j) PL spectra decomposed into bright exciton (red) and dark exciton (blue) PL at 5 K shown in (a) and (b). (k) Effect of electronic coupling on bright and dark exciton PL decay and energetics and ΔE_{BD}. Reprinted with permission from Tang, X. et al. *Chem. Mater.* **2022**, *34*, 7181-7189. Copyright 2022 American Chemical Society.

Figure 28 compares the time-dependent PL spectra (a-d) and time-dependent PL intensity (e-h) of the arrays of OLAB- and NaBr-passivated l=3.8 nm QDs at 5 K, which allows to examine the effect of electronic coupling on the relative energy level and dynamics of bright and dark exciton. To show the behavior of bright and dark exciton

separately, the time-dependent PL are shown in two different time windows: 30 μs and 5 ns. Figure 28i and j are the time-integrated PL spectra and fit to the sum of bright and dark exciton PL spectra for the arrays of OLAB- and NaBr-passivated QDs respectively. At the temperatures sufficiently low, where the thermal energy (kT) is much smaller than bright-dark splitting energy (ΔE_{BD}), emission from dark exciton level can be readily observed due to the suppression of thermal excitation from dark to bright state.[8] Time-dependent PL spectra and PL intensity in Figure 28a, b, e and f show dark exciton PL decaying on μs time scale (τ_D), well-separated from the fast decay component (τ_{fast}) attributed to the decay of bright exciton PL. Fast decay component is more clearly seen in Figure 28c and d. τ_{fast} has two contributions, one from relaxation of bright exciton and the other from bright-to-dark transition[8].

Since the τ_{fast} and τ_D differ by 4 orders of magnitude, bright and dark exciton PL spectra can be readily separated by time-gating the PL as shown in Figure 28i and j, from which ΔE_{BD} can be extracted. In Figure 28j, a shoulder peak near 500 nm that was assigned to merged QDs in the steady state PL shown in Figure 24a also appears, but less well resolved than in the steady state PL spectra due to the difference in the spectral resolution of the two spectrometers. Table 7 summarizes ΔE_{BD}, τ_D and τ_{fast} obtained from the data in Figure 28. The fraction of photons emitted from dark state in the overall PL (I_D/I_{total}) at 5 K determined from the data in Figure 28e, f, i and j is also added in Table 7.

Table 7 Parameters extracted from 5 K PL decay data. λ_B and λ_D are PL wavelength for bright and dark exciton, ΔE_{BD} is bright-dark energy splitting, τ_D and τ_{fast} are the time constants for the dark exciton PL and fast-decaying PL respectively. I_D/I_{total} is the fraction of photons emitted from dark exciton in the total PL at 5 K. Reprinted with permission from Tang, X. et al. *Chem. Mater.* **2022**, *34*, 7181-7189. Copyright 2022 American Chemical Society.

Ligand	λ_B	λ_D	ΔE_{BD}	I_D/I_{total}	τ_D	τ_{fast}
OLAB	471.7 nm	476.4 nm	25 meV	65 %	12 μs	0.42 ns
NaBr	480.3 nm	483.4 nm	16 meV	34 %	9 μs	0.29 ns

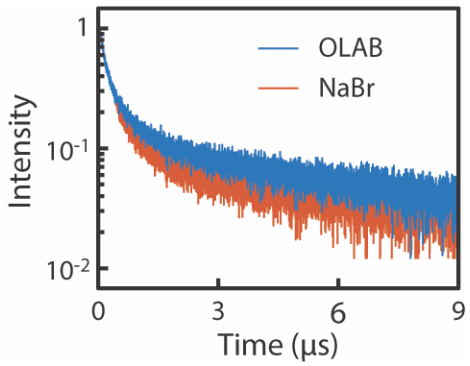

Figure 29 Time-dependent PL intensities of the arrays of *l*=4.2 nm $CsPbBr_3$ QDs passivated with OLAB (blue) and NaBr (red) at 5 K. The dark exciton lifetime is 8.4 and 8.1 μs respectively for OLAB- and NaBr-passivated QDs. Reprinted with permission from Tang, X. et al. *Chem. Mater.* **2022**, *34*, 7181-7189. Copyright 2022 American Chemical Society.

The main effect of electronic coupling in the array of NaBr-passivated l=3.8 nm QDs clearly observed from the data in Figure 28 are the decrease of ΔE_{BD}, τ_D and τ_{fast} compared to the array of OLAB-passivated QDs. This contrasts with the behavior of NaBr-passivated l=4.2 nm QDs that exhibit the much weaker electronic coupling. For instance, τ_D of the arrays of OLAB- and NaBr-passivated l=4.2 nm QDs are 8.4 μs and 8.1 μs respectively, showing much weaker effect on the decay rate of dark exciton compared to l=3.8 nm QDs, as shown in Figure 29.

In our recent study of the PL from non-interacting $CsPbBr_3$ QDs of different sizes dispersed in polymer matrix, decrease of ΔE_{BD} and τ_D were observed with increasing QD size.[46] The weaker electron-hole exchange interaction in the less confined QDs was considered responsible for the decreasing ΔE_{BD} with increasing QD size.[38, 46] In the presence of perturbations that can mix bright and dark states in semiconductor QDs, such as spin-orbit coupling, surface or defect spins, and optical/acoustic phonons, the mixing of bright and dark states is expected to increase with decrease in ΔE_{BD}.[38, 123-125] Therefore, the decrease of ΔE_{BD} in the electronically coupled array of QDs can be interpreted as the result of the increased spatial extent of electron and hole wavefunction via electronic coupling that reduces the electron-hole exchange interaction. This suggests that changes in relative energies of bright and dark exciton level can be explained by the delocalization of exciton wavefunction via electronic coupling in the array of QDs, which is similar to the effects of increasing the QD size in non-interacting ensemble. The decrease of τ_D by electronic coupling is also consistent with the smaller ΔE_{BD} observed in the larger non-interacting QDs. Previous studies showed approximately linear slope of ΔE_{BD} vs inverse

volume for the cube-shaped perovskite QDs consistent with the theoretical prediction.[38, 41, 46] ΔE_{BD} was also found to decrease with increasing thickness in nanoplatelets.[90] The direct comparison of the effect of size increase in uncoupled QDs and delocalization of exciton limited to the lateral direction in 2D array of the coupled QDs will not be quantitatively valid. However, comparison with the size-dependent ΔE_{BD} reported in Reference [46] indicates that the change of ΔE_{BD} observed in the coupled QDs in this study is equivalent to the volume increase of ~50% in uncoupled QDs.

It is interesting to note that τ_{fast} at 5 K is smaller in NaBr-passivated QDs than in OLAB-passivated QDs, which contrasts to the slower bright exciton relaxation on ns time scale at 300 K in NaBr-passivated QDs (τ=8.8 ns) than in OLAB-passivated QDs (τ=4.2 ns) as shown in Figure 22. τ_{fast} at 5 K reflects the time constant for the combined processes of bright exciton relaxation and bright-dark transition.[46] Therefore, the shortening of τ_{fast} in NaBr-passivated QDs can have multiple contributions. While the PL quantum yield at 5 K is uncertain due to the difficulty in accurately quantifying the PL intensity from the QD arrays assembled on a TEM grid in vacuum, we consider the contribution from the nonradiative decay is minimal at this low temperature. Since the PL from dark exciton with ~10 μs can be readily observed and that the relative PL intensity increases with temperature decrease, as shown in Figure 30, we consider the thermally activated trapping of exciton leading to nonradiative decay is effectively suppressed at 5 K.

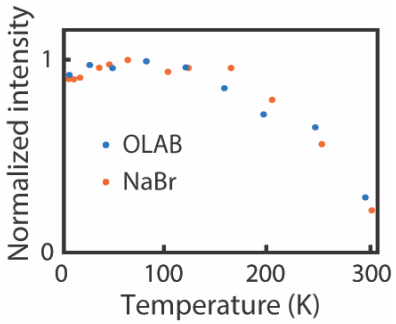

Figure 30 Temperature-dependent PL intensity of OLAB- and NaBr-passivated QDs, with the intensity normalized to 1 based on the maximum intensity. Reprinted with permission from Tang, X. et al. *Chem. Mater.* **2022**, *34*, 7181-7189. Copyright 2022 American Chemical Society.

Under the assumption that excludes the nonradiative decay pathways of exciton, one possible contribution to the shortening of τ_{fast} is the giant oscillator strength transition effect that accelerates the bright exciton emission. A recent study in perovskite nanocrystals indicated that the faster radiative recombination of bright exciton is expected at the lower temperature due to the giant oscillator strength transition of the exciton, which is more prominent in the larger and less confined QDs.[39] The increase in exciton oscillator strength upon cooling from the giant oscillator transition strength effect via coherent center-of-mass delocalization of exciton has also been reported in CdSe nanoplatelets.[41] The effect of electronic coupling in the 2D array of the QDs on the temperature-dependent oscillator strength may be similar to that of increasing the size of the QDs. Presently, such possibility cannot be directly confirmed from the temperature-dependent absorption spectra due to the difficulty in measuring the absorption from a 2D array of the QDs.

However, studies in the coupled 3D superlattice, whose temperature-dependent absorption may be easier to quantify, could shed more light on this issue. In addition, whether the electronic coupling will affect the bright-dark transition rate is another remaining question that will require further study.

4.4. Conclusion

In conclusion, we investigated the effect of electronic coupling between strongly quantum confined $CsPbBr_3$ QDs on the energetics and dynamics of bright and dark exciton. For this purpose, close-packed 2D arrays of QDs with facet-to-facet distance reduced to several Å were prepared via ligand replacement from OLAB to NaBr. Comparison of the steady state and time-dependent PL spectra of the arrays of OLAB- and NaBr-passivated QDs in a wide range of temperatures showed that bright-dark energy splitting decreases in addition to the redshift of both bright and dark levels compared to non-interacting array of the QDs. The dynamics of bright and dark exciton relaxation at 5 K also accelerates in the electronically coupled array of the QDs. These observations are consistent with the delocalization of exciton wavefunction beyond a single QD in the coupled ensemble of the QDs, where the net effect is similar to increasing the volume of the non-interacting QDs.

5. CHAPTER V

SUMMARY AND FUTURE OUTLOOK

5.1. PL Properties of Strongly Quantum-Confined $FAPbBr_3$ QDs

In this project, we investigated the effect of strong quantum confinement on the photophysical properties of $FAPbBr_3$ QDs. For this purpose, we firstly developed the synthetic strategy for strongly quantum-confined $FAPbBr_3$ QDs with tunable sizes in the range of 3-6 nm by changing the reaction temperature. The product $FAPbBr_3$ QDs showed uniform cubic morphology as well as great size distribution of less than 5%. Absorption and PL spectra of the strongly quantum-confined $FAPbBr_3$ QDs at room temperature demonstrated effect of the strong quantum confinement, by showing the increasing band gap with decreasing QD size. The PLQY and time resolved PL intensity of $FAPbBr_3$ QDs of different sizes did not show significant differences, suggesting that the quantum confinement do not play a part on the single exciton decay rate at room temperature.

Afterwards, PL measurement were further carried out at cryogenic temperature to investigate the effect of quantum confinement on the exciton PL properties and exciton fine structure. When the temperature decreased from 295 K to 78 K, PL spectra of $FAPbBr_3$ QDs showed continuous redshift and linewidth narrowing. This observation is comparable to the behavior of $CsPbBr_3$ QDs, where the PL redshift and linewidth narrowing were attributed to lattice contraction and electron-phonon coupling.

Time-resolved PL spectra of $FAPbBr_3$ QDs at 5 K observed intense PL from dark lowest-energy exciton state with μs lifetime. For the different sizes of $FAPbBr_3$ QDs studied, the smaller QDs exhibited both longer dark exciton lifetime and larger bright-

dark level energy splitting, ΔE_{BD}. This observation is in consistent with the previous computational and experimental reports on $CsPbBr_3$ QDs, suggesting that the model where the ΔE_{BD} related to the electron-hole exchange increases with increasing quantum confinement is also applicable in the $FAPbBr_3$ QDs.

The magnetic field strength dependence of the dark exciton dynamics is then investigated. The results showed that the dark exciton lifetime, τ_D, is less significant in smaller $FAPbBr_3$ QD size, as expected. However, one interesting observation is that, the dependence of τ_D on the magnetic field strength was less significant in $FAPbBr_3$ QDs compared to $CsPbBr_3$ QDs, with the smallest 3.7 nm $FAPbBr_3$ QDs showing negligible dependence on the magnetic field strength. The reason for their reduced response to the magnetic field is still unknown, making it an interesting topic for further explorations.

5.2. Effects of Electronic Coupling on 2D Arrays of $CsPbBr_3$ QDs

In this project, we investigated the effect of inter-QD electronic coupling on the photophysical properties of strong quantum confined $CsPbBr_3$ QDs. For this purpose, we first synthesized strongly quantum confined $CsPbBr_3$ QDs with sizes in the range of 3.8-5.3 nm. Then, we carried out ligand exchange on the $CsPbBr_3$ QDs, where the original OLAB ligands were replaced by NaBr. The product QDs showed remarkably reduced interparticle distance by over 2 nm after the ligand exchange procedure. Afterwards, 2D arrays of $CsPbBr_3$ QDs with sub-nm facet-to-facet distance were prepared by drop-casting the QD colloidal solution onto TEM grids.

We then investigated the photophysical properties of these electronic coupled arrays of $CsPbBr_3$ QDs through PL spectroscopy and dynamics, and compared these

properties to the non-coupled arrays of $CsPbBr_3$ QDs passivated with OLAB ligands as well. At room temperature, the coupled arrays of $CsPbBr_3$ QDs showed PL redshift and linewidth narrowing as compared to the uncoupled ones, with more redshift and linewidth narrowing observed in smaller QDs as a result of the increased coupling energy with stronger quantum confinement. The coupled arrays also exhibited slower exciton recombination rates as compared to the noncoupled ones, suggesting increased exciton delocalization in the presence of electronic coupling.

Furthermore, the PL spectra and dynamics were then investigated at cryogenic temperature for the exploration of the energetics and dynamics of bright and dark exciton in electronically coupled arrays of $CsPbBr_3$ QDs. Compared to noncoupled arrays of QDs, coupled ones showed a decrease in the bright-dark energy splitting, ΔE_{BD} as well as the dark exciton lifetime, τ_D. These observations suggest that the exciton delocalization is increased in electronically coupled arrays of $CsPbBr_3$ QDs, where the net effect is similar to increasing the volume of the non-interacting QDs.

Interestingly, at cryogenic temperature, the bright exciton lifetime, τ_B, was also observed to be shorter in electronically coupled array of $CsPbBr_3$ QDs as compared to the noncoupled ones. This is opposite to the observation at room temperature. The increase in τ_B could be potentially explain with the giant oscillator strength transition effect, where the optical transitions are significantly enhanced when the oscillator strength are increased due to exciton delocalization covering more unit cells of materials. This observation is highly promising for QD lasers, which can be a potential interesting topic for further explorations.

5.3. Future Outlook on 3D Electronic Coupled Superlattices of Strongly Quantum Confined $CsPbBr_3$ QDs

Many research studies have reported spontaneous assembly of LHP NCs into highly ordered structures known as superlattices (SLs)[106, 107, 110, 111, 126]. The formation of the SLs typically takes place during the evaporation of the solvents, during which the highly uniform cubic LHP NCs assemble into ordered arrays driven by the inter-NC forces. The narrow size distribution of the LHP NCs is an essential factor for the formation of NC SLs with long rage order. As compared to isolated NCs, the NCs within the SLs exhibited new photophysical properties arise from the collective electronic or photonic activity of the NCs, making them an interesting topic to investigate.

The most straightforward optical property of LHP NCs SLs is the redshifted PL spectra as compared to the isolated ones. At room temperature, the PL redshift of SLs by several meV compared to solution phase NCs has been observed in multiple studies in weakly quantum confined NCs[106-108]. A detailed study on the origin of this PL redshift attributed it to a combined effect of electronic coupling, energy transfer between NC inhomogeneity and loss of quantum confinement due to NC merging and aggregation[110, 127].

More interestingly, these SLs are reported to exhibit coherent emission at under excitation. The first report of coherent emission of SLs of LHP NCs was in weakly quantum confined $CsPbBr_3$ NCs with a mean size of 9.5 nm[111]. In this study, the SLs exhibited extremely narrow PL emission with the peak position redshifted over 70 meV and radiative decay rate accelerated by almost 3 times at 6 K under high power excitation.

These observations were attributed to the coherent emission established from the ordered transition dipoles of NCs in the SLs aligned by the emission photon field. Later, a following study reported similar observations of PL narrowing, redshift and acceleration at 77 K in SL microcavities[128]. In this study, the investigation on the cooperative optical properties of the SLs further revealed enhanced stimulated emission efficiency in the SL microcavities where the stimulated emission relies on the phasing of the transition dipoles rather than the population inversion. More recently, the coherent emission studies have been extended to SLs of organic-inorganic hybrid LHP NCs, where superfluorescence was observed at higher temperature, even at room temperature[129, 130]. The degree of the coherence is reported to be largely dependent on the size uniformity and the ordering of the NC SLs[131], where the information can be extracted from small-angle X-ray scattering and wide-angle X-ray scattering[126, 132].

Aside from the reports of superfluorescence in LHP NC SLs, one recent research paper reported the observations of superradiance in SLs of 9 nm $CsPbBr_3$ NCs below 78 K, characterized by narrow and redshifted PL with accelerated decay rate, similar to the previous reports about superfluorescence[133]. Superfluorescence and superradiance are both coherent emission of multiple emitters, but their difference is defined by the stage when the coherence is formed. In the case of superradiance, the coherence is formed before the emission, whereas in the case of superfluorescence, the coherence is formed during the emission. In this study, the origin of the coherence of the NCs in the SLs was claimed to be a result of the inter-NC electronic coupling, even though electronic coupling of this system should be almost negligible based on our experimental results stated in Chapter III.

Nonetheless, this work suggests the promising future studies of utilization of superradiance in strongly quantum confined QDs and 3D electronically coupled arrays of them.

For this objective, some testing experiments have been carried out on strongly quantum confined $CsPbBr_3$ NCs and the preliminary results of PL spectra at cryogenic temperature showed features of superradiance. Firstly, the SLs were fabricated with 4 nm $CsPbBr_3$ QDs passivated with original OLAB ligands through self-assembly during solvent evaporation. Specifically, the QDs were synthesized and purified following the method in Reference 19. After the final precipitation with acetone, the precipitate was dispensed into a small amount of hexane to obtain a high-concentration stock solution with an absorbance of over 100 at 400 nm for 1 cm pathlength. A small amount of the stock solution was then diluted with cyclooctane to an absorbance of 5 at 400 nm for the SL growth. 10 μL of the diluted QD/cyclooctane solution was drop-casted onto a slide of silicon wafer placed in a 1 inch ×1 inch Teflon well. Then, the Teflon well was partially isolated from the ambient environment by placing a glass slide on top of the well as a lid. This setup was left in an N_2 environment at room temperature for 24-72 hours until the solvent evaporated completely.

As the results of the SL solvent evaporation, the QDs spontaneously assembles into superstructures with sizes on the μm scale, forming two types of different assemblies, as shown in Figure 31. Firstly, large rhombic SLs of the $CsPbBr_3$ QDs with edge sizes on the order of 10 μm were observed in both Scanning Electron Microscopy (SEM) and Confocal Microscopy (CM) images, similar to other reported works of SLs of the strongly

quantum confined $CsPbBr_3$ QDs[134]. The rhombic shape of the SLs was attributed to the tendency for higher packing density favored by the softer small QDs as compared to the larger weakly quantum confined NCs that favors cubic packing. Meanwhile, smaller cuboidal SLs and multi-crystalline clusters of them were also observed with edge lengths on the order of 100 nm – 1 μm.

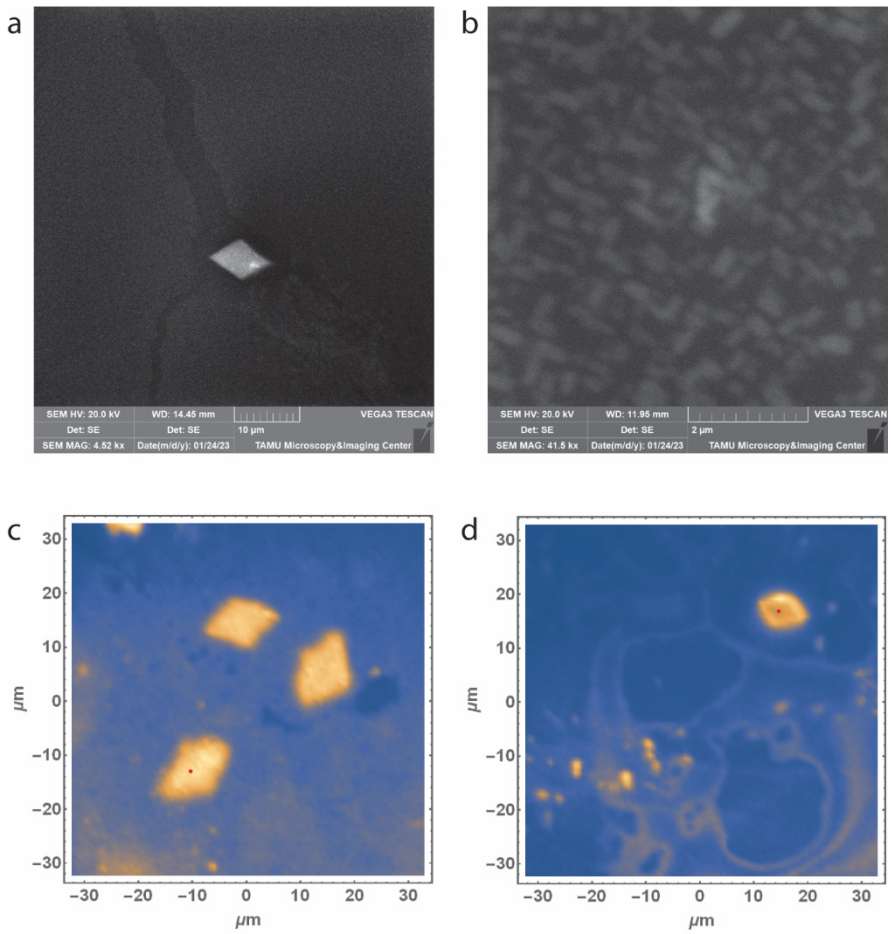

Figure 31 (a, b) SEM images of SLs of the 4 nm $CsPbBr_3$ QDs in different regions showing large and small SLs, respectively. (c, d) CM images of SLs of the 4 nm $CsPbBr_3$ QDs in different regions.

Following up, spectroscopic experiments were carried out in the CM setup, where the PL spectra of the individual SLs were measured at room and cryogenic temperatures. At room temperature, similar to SLs of weakly quantum confined NCs, redshift and linewidth narrowing of the PL was observed for both small and large SLs as compared to the background of randomly distributed QDs. At ~10 K, extremely narrow PL linewidth of ~10 meV was observed for some of the large multi-crystalline SL clusters, as compared to the ~40 meV linewidth in the large SLs, randomly distributed QDs and isolated small SLs. This is a signature of superradiance emission. However, PL blueshift was observed for these large multi-crystalline SL clusters compared to in other regions. However, the origin of this blueshift is unknown yet, and further studies will be carried out in order to study the potential mechanism of superradiance in SLs of strongly quantum confined $CsPbBr_3$ QDs.

REFERENCES

1. Kojima, A.; Teshima, K.; Shirai, Y.; Miyasaka, T., Organometal Halide Perovskites as Visible-Light Sensitizers for Photovoltaic Cells. *J. Am. Chem. Soc.* **2009,** *131* (17), 6050-6051.

2. Kim, H. S.; Lee, C. R.; Im, J. H.; Lee, K. B.; Moehl, T.; Marchioro, A.; Moon, S. J.; Humphry-Baker, R.; Yum, J. H.; Moser, J. E.; Gratzel, M.; Park, N. G., Lead Iodide Perovskite Sensitized All-Solid-State Submicron Thin Film Mesoscopic Solar Cell with Efficiency Exceeding 9%. *Sci. Rep.* **2012,** *2*, 591.

3. Lee, M. M.; Teuscher, J.; Miyasaka, T.; Murakami, T. N.; Snaith, H. J., Efficient Hybrid Solar Cells Based on Meso-Superstructured Organometal Halide Perovskites. *Science* **2012,** *338* (6107), 643-647.

4. Li, L.; Wang, Y.; Wang, X.; Lin, R.; Luo, X.; Liu, Z.; Zhou, K.; Xiong, S.; Bao, Q.; Chen, G.; Tian, Y.; Deng, Y.; Xiao, K.; Wu, J.; Saidaminov, M. I.; Lin, H.; Ma, C.-Q.; Zhao, Z.; Wu, Y.; Zhang, L., et al., Flexible all-perovskite tandem solar cells approaching 25% efficiency with molecule-bridged hole-selective contact. *Nat. Energy* **2022,** *7* (8), 708-717.

5. Zhang, Q.; Shang, Q.; Su, R.; Do, T. T. H.; Xiong, Q., Halide Perovskite Semiconductor Lasers: Materials, Cavity Design, and Low Threshold. *Nano Lett.* **2021,** *21* (5), 1903-1914.

6. Quan, L. N.; Rand, B. P.; Friend, R. H.; Mhaisalkar, S. G.; Lee, T. W.; Sargent, E. H., Perovskites for Next-Generation Optical Sources. *Chem. Rev.* **2019,** *119* (12), 7444-7477.

7. Zhang, H.; Fu, X.; Tang, Y.; Wang, H.; Zhang, C.; Yu, W. W.; Wang, X.; Zhang, Y.; Xiao, M., Phase Segregation due to Ion Migration in All-Inorganic Mixed-Halide Perovskite Nanocrystals. *Nat. Commun.* **2019,** *10* (1), 1088.

8. Rossi, D.; Liu, X.; Lee, Y.; Khurana, M.; Puthenpurayil, J.; Kim, K.; Akimov, A. V.; Cheon, J.; Son, D. H., Intense Dark Exciton Emission from Strongly Quantum-Confined $CsPbBr_3$ Nanocrystals. *Nano Lett.* **2020,** *20* (10), 7321-7326.

9. Cheng, O. H.; Qiao, T.; Sheldon, M.; Son, D. H., Size- and temperature-dependent photoluminescence spectra of strongly confined $CsPbBr_3$ quantum dots. *Nanoscale* **2020,** *12* (24), 13113-13118.

10. Protesescu, L.; Yakunin, S.; Bodnarchuk, M. I.; Krieg, F.; Caputo, R.; Hendon, C. H.; Yang, R. X.; Walsh, A.; Kovalenko, M. V., Nanocrystals of Cesium Lead Halide Perovskites ($CsPbX_3$, X = Cl, Br, and I): Novel Optoelectronic Materials Showing Bright Emission with Wide Color Gamut. *Nano Lett.* **2015,** *15* (6), 3692-3696.

11. Amgar, D.; Binyamin, T.; Uvarov, V.; Etgar, L., Near Ultra-Violet to Mid-Visible Band Gap Tuning of Mixed Cation $Rb_xCs_{1-x}PbX_3$ (X = Cl or Br) perovskite nanoparticles. *Nanoscale* **2018,** *10* (13), 6060-6068.

12. Protesescu, L.; Yakunin, S.; Bodnarchuk, M. I.; Bertolotti, F.; Masciocchi, N.; Guagliardi, A.; Kovalenko, M. V., Monodisperse Formamidinium Lead Bromide Nanocrystals with Bright and Stable Green Photoluminescence. *J. Am. Chem. Soc.* **2016,** *138* (43), 14202-14205.

13. Protesescu, L.; Yakunin, S.; Kumar, S.; Bar, J.; Bertolotti, F.; Masciocchi, N.; Guagliardi, A.; Grotevent, M.; Shorubalko, I.; Bodnarchuk, M. I.; Shih, C. J.;

Kovalenko, M. V., Dismantling the "Red Wall" of Colloidal Perovskites: Highly Luminescent Formamidinium and Formamidinium-Cesium Lead Iodide Nanocrystals. *ACS Nano* **2017,** *11* (3), 3119-3134.

14. Bekenstein, Y.; Koscher, B. A.; Eaton, S. W.; Yang, P.; Alivisatos, A. P., Highly Luminescent Colloidal Nanoplates of Perovskite Cesium Lead Halide and Their Oriented Assemblies. *J. Am. Chem. Soc.* **2015,** *137* (51), 16008-16011.

15. Almeida, G.; Goldoni, L.; Akkerman, Q.; Dang, Z.; Khan, A. H.; Marras, S.; Moreels, I.; Manna, L., Role of Acid-Base Equilibria in the Size, Shape, and Phase Control of Cesium Lead Bromide Nanocrystals. *ACS Nano* **2018,** *12* (2), 1704-1711.

16. Udayabhaskararao, T.; Kazes, M.; Houben, L.; Lin, H.; Oron, D., Nucleation, Growth, and Structural Transformations of Perovskite Nanocrystals. *Chem. Mater.* **2017,** *29* (3), 1302-1308.

17. Lignos, I.; Stavrakis, S.; Nedelcu, G.; Protesescu, L.; deMello, A. J.; Kovalenko, M. V., Synthesis of Cesium Lead Halide Perovskite Nanocrystals in a Droplet-Based Microfluidic Platform: Fast Parametric Space Mapping. *Nano Lett.* **2016,** *16* (3), 1869-1877.

18. Koolyk, M.; Amgar, D.; Aharon, S.; Etgar, L., Kinetics of Cesium Lead Halide Perovskite Nanoparticle Growth; Focusing and De-focusing of Size Distribution. *Nanoscale* **2016,** *8* (12), 6403-6409.

19. Dong, Y.; Qiao, T.; Kim, D.; Parobek, D.; Rossi, D.; Son, D. H., Precise Control of Quantum Confinement in Cesium Lead Halide Perovskite Quantum Dots via Thermodynamic Equilibrium. *Nano Lett.* **2018,** *18* (6), 3716-3722.

20. Zhang, F.; Zhong, H.; Chen, C.; Wu, X. G.; Hu, X.; Huang, H.; Han, J.; Zou, B.; Dong, Y., Brightly Luminescent and Color-Tunable Colloidal $CH_3NH_3PbX_3$ (X = Br, I, Cl) Quantum Dots: Potential Alternatives for Display Technology. *ACS Nano* **2015,** *9* (4), 4533-4542.

21. Huang, H.; Susha, A. S.; Kershaw, S. V.; Hung, T. F.; Rogach, A. L., Control of Emission Color of High Quantum Yield $CH_3NH_3PbBr_3$ Perovskite Quantum Dots by Precipitation Temperature. *Adv. Sci.* **2015,** *2* (9), 1500194.

22. Minh, D. N.; Kim, J.; Hyon, J.; Sim, J. H.; Sowlih, H. H.; Seo, C.; Nam, J.; Eom, S.; Suk, S.; Lee, S.; Kim, E.; Kang, Y., Room-Temperature Synthesis of Widely Tunable Formamidinium Lead Halide Perovskite Nanocrystals. *Chem. Mater.* **2017,** *29* (13), 5713-5719.

23. Weidman, M. C.; Seitz, M.; Stranks, S. D.; Tisdale, W. A., Highly Tunable Colloidal Perovskite Nanoplatelets through Variable Cation, Metal, and Halide Composition. *ACS Nano* **2016,** *10* (8), 7830-7839.

24. De Roo, J.; Ibanez, M.; Geiregat, P.; Nedelcu, G.; Walravens, W.; Maes, J.; Martins, J. C.; Van Driessche, I.; Kovalenko, M. V.; Hens, Z., Highly Dynamic Ligand Binding and Light Absorption Coefficient of Cesium Lead Bromide Perovskite Nanocrystals. *ACS Nano* **2016,** *10* (2), 2071-2081.

25. Pan, J.; Quan, L. N.; Zhao, Y.; Peng, W.; Murali, B.; Sarmah, S. P.; Yuan, M.; Sinatra, L.; Alyami, N. M.; Liu, J.; Yassitepe, E.; Yang, Z.; Voznyy, O.; Comin, R.; Hedhili, M. N.; Mohammed, O. F.; Lu, Z. H.; Kim, D. H.; Sargent, E. H.; Bakr, O. M.,

Highly Efficient Perovskite-Quantum-Dot Light-Emitting Diodes by Surface Engineering. *Adv. Mater. (Weinheim, Ger.)* **2016,** *28* (39), 8718-8725.

26. Bodnarchuk, M. I.; Boehme, S. C.; Ten Brinck, S.; Bernasconi, C.; Shynkarenko, Y.; Krieg, F.; Widmer, R.; Aeschlimann, B.; Gunther, D.; Kovalenko, M. V.; Infante, I., Rationalizing and Controlling the Surface Structure and Electronic Passivation of Cesium Lead Halide Nanocrystals. *ACS Energy Lett.* **2019,** *4* (1), 63-74.

27. Nenon, D. P.; Pressler, K.; Kang, J.; Koscher, B. A.; Olshansky, J. H.; Osowiecki, W. T.; Koc, M. A.; Wang, L. W.; Alivisatos, A. P., Design Principles for Trap-Free $CsPbX_3$ Nanocrystals: Enumerating and Eliminating Surface Halide Vacancies with Softer Lewis Bases. *J. Am. Chem. Soc.* **2018,** *140* (50), 17760-17772.

28. Vickers, E. T.; Graham, T. A.; Chowdhury, A. H.; Bahrami, B.; Dreskin, B. W.; Lindley, S.; Naghadeh, S. B.; Qiao, Q. Q.; Zhang, J. Z., Improving Charge Carrier Delocalization in Perovskite Quantum Dots by Surface Passivation with Conductive Aromatic Ligands. *ACS Energy Lett.* **2018,** *3* (12), 2931-2939.

29. Dong, Y.; Wang, Y. K.; Yuan, F.; Johnston, A.; Liu, Y.; Ma, D.; Choi, M. J.; Chen, B.; Chekini, M.; Baek, S. W.; Sagar, L. K.; Fan, J.; Hou, Y.; Wu, M.; Lee, S.; Sun, B.; Hoogland, S.; Quintero-Bermudez, R.; Ebe, H.; Todorovic, P., et al., Bipolar-Shell Resurfacing for Blue LEDs Based on Strongly Confined Perovskite Quantum Dots. *Nat. Nanotechnol.* **2020,** *15* (8), 668-674.

30. Yang, J. N.; Song, Y.; Yao, J. S.; Wang, K. H.; Wang, J. J.; Zhu, B. S.; Yao, M. M.; Rahman, S. U.; Lan, Y. F.; Fan, F. J.; Yao, H. B., Potassium Bromide Surface

Passivation on $CsPbI_{3-x}Br_x$ Nanocrystals for Efficient and Stable Pure Red Perovskite Light-Emitting Diodes. *J. Am. Chem. Soc.* **2020,** *142* (6), 2956-2967.

31. Krieg, F.; Ochsenbein, S. T.; Yakunin, S.; Ten Brinck, S.; Aellen, P.; Suess, A.; Clerc, B.; Guggisberg, D.; Nazarenko, O.; Shynkarenko, Y.; Kumar, S.; Shih, C. J.; Infante, I.; Kovalenko, M. V., Colloidal $CsPbX_3$ (X = Cl, Br, I) Nanocrystals 2.0: Zwitterionic Capping Ligands for Improved Durability and Stability. *ACS Energy Lett.* **2018,** *3* (3), 641-646.

32. Filip, M. R.; Eperon, G. E.; Snaith, H. J.; Giustino, F., Steric Engineering of Metal-Halide Perovskites with Tunable Optical Band Gaps. *Nat. Commun.* **2014,** *5*, 5757.

33. Sichert, J. A.; Tong, Y.; Mutz, N.; Vollmer, M.; Fischer, S.; Milowska, K. Z.; Garcia Cortadella, R.; Nickel, B.; Cardenas-Daw, C.; Stolarczyk, J. K.; Urban, A. S.; Feldmann, J., Quantum Size Effect in Organometal Halide Perovskite Nanoplatelets. *Nano Lett.* **2015,** *15* (10), 6521-7.

34. Akkerman, Q. A.; Motti, S. G.; Srimath Kandada, A. R.; Mosconi, E.; D'Innocenzo, V.; Bertoni, G.; Marras, S.; Kamino, B. A.; Miranda, L.; De Angelis, F.; Petrozza, A.; Prato, M.; Manna, L., Solution Synthesis Approach to Colloidal Cesium Lead Halide Perovskite Nanoplatelets with Monolayer-Level Thickness Control. *J. Am. Chem. Soc.* **2016,** *138* (3), 1010-1016.

35. Li, Y.; Ding, T.; Luo, X.; Tian, Y.; Lu, X.; Wu, K., Synthesis and Spectroscopy of Monodispersed, Quantum-Confined $FAPbBr_3$ Perovskite Nanocrystals. *Chem. Mater.* **2019,** *32* (1), 549-556.

36. Brennan, M. C.; Herr, J. E.; Nguyen-Beck, T. S.; Zinna, J.; Draguta, S.; Rouvimov, S.; Parkhill, J.; Kuno, M., Origin of the Size-Dependent Stokes Shift in $CsPbBr_3$ Perovskite Nanocrystals. *J. Am. Chem. Soc.* **2017,** *139* (35), 12201-12208.

37. Efros, A. L.; Rosen, M.; Kuno, M.; Nirmal, M.; Norris, D. J.; Bawendi, M., Band-Edge Exciton in Quantum Dots of Semiconductors With a Degenerate Valence Band: Dark and Bright Exciton States. *Phys. Rev. B: Condens. Matter* **1996,** *54* (7), 4843-4856.

38. Leung, K.; Pokrant, S.; Whaley, K. B., Exciton Fine Structure in CdSe Nanoclusters. *Phys. Rev. B* **1998,** *57* (19), 12291-12301.

39. Becker, M. A.; Vaxenburg, R.; Nedelcu, G.; Sercel, P. C.; Shabaev, A.; Mehl, M. J.; Michopoulos, J. G.; Lambrakos, S. G.; Bernstein, N.; Lyons, J. L.; Stoferle, T.; Mahrt, R. F.; Kovalenko, M. V.; Norris, D. J.; Raino, G.; Efros, A. L., Bright Triplet Excitons in Caesium Lead Halide Perovskites. *Nature* **2018,** *553* (7687), 189-193.

40. Isarov, M.; Tan, L. Z.; Bodnarchuk, M. I.; Kovalenko, M. V.; Rappe, A. M.; Lifshitz, E., Rashba Effect in a Single Colloidal $CsPbBr_3$ Perovskite Nanocrystal Detected by Magneto-Optical Measurements. *Nano Lett.* **2017,** *17* (8), 5020-5026.

41. Sercel, P. C.; Lyons, J. L.; Wickramaratne, D.; Vaxenburg, R.; Bernstein, N.; Efros, A. L., Exciton Fine Structure in Perovskite Nanocrystals. *Nano Lett.* **2019,** *19* (6), 4068-4077.

42. Canneson, D.; Shornikova, E. V.; Yakovlev, D. R.; Rogge, T.; Mitioglu, A. A.; Ballottin, M. V.; Christianen, P. C. M.; Lhuillier, E.; Bayer, M.; Biadala, L., Negatively

Charged and Dark Excitons in $CsPbBr_3$ Perovskite Nanocrystals Revealed by High Magnetic Fields. *Nano Lett.* **2017,** *17* (10), 6177-6183.

43. Fu, M.; Tamarat, P.; Huang, H.; Even, J.; Rogach, A. L.; Lounis, B., Neutral and Charged Exciton Fine Structure in Single Lead Halide Perovskite Nanocrystals Revealed by Magneto-optical Spectroscopy. *Nano Lett.* **2017,** *17* (5), 2895-2901.

44. Tamarat, P.; Bodnarchuk, M. I.; Trebbia, J. B.; Erni, R.; Kovalenko, M. V.; Even, J.; Lounis, B., The Ground Exciton State of Formamidinium Lead Bromide Perovskite Nanocrystals is a Singlet Dark State. *Nat. Mater.* **2019,** *18* (7), 717-724.

45. Chen, L.; Li, B.; Zhang, C.; Huang, X.; Wang, X.; Xiao, M., Composition-Dependent Energy Splitting between Bright and Dark Excitons in Lead Halide Perovskite Nanocrystals. *Nano Lett.* **2018,** *18* (3), 2074-2080.

46. Rossi, D.; Qiao, T.; Liu, X.; Khurana, M.; Akimov, A. V.; Cheon, J.; Son, D. H., Size-Dependent Dark Exciton Properties in Cesium Lead Halide Perovskite Quantum Dots. *J. Chem. Phys.* **2020,** *153* (18), 184703.

47. Rudin, S.; Reinecke, T. L.; Segall, B., Temperature-Dependent Exciton Linewidths in Semiconductors. *Phys. Rev. B: Condens. Matter* **1990,** *42* (17), 11218-11231.

48. Saran, R.; Heuer-Jungemann, A.; Kanaras, A. G.; Curry, R. J., Giant Bandgap Renormalization and Exciton-Phonon Scattering in Perovskite Nanocrystals. *Adv. Opt. Mater.* **2017,** *5* (17), 1700231.

49. Ramade, J.; Andriambariarijaona, L. M.; Steinmetz, V.; Goubet, N.; Legrand, L.; Barisien, T.; Bernardot, F.; Testelin, C.; Lhuillier, E.; Bramati, A.; Chamarro, M.,

Exciton-Phonon Coupling in a $CsPbBr_3$ Single Nanocrystal. *Appl. Phys. Lett.* **2018,** *112* (7).

50. Diroll, B. T.; Zhou, H.; Schaller, R. D., Low‐Temperature Absorption, Photoluminescence, and Lifetime of $CsPbX_3$ (X = Cl, Br, I) Nanocrystals. *Adv. Funct. Mater.* **2018,** *28* (30).

51. Li, J. M.; Yuan, X.; Jing, P. T.; Li, J.; Wei, M. B.; Hua, J.; Zhao, J. L.; Tian, L. H., Temperature-Dependent Photoluminescence of Inorganic Perovskite Nanocrystal Films. *RSC Adv.* **2016,** *6* (82), 78311-78316.

52. Strandell, D. P.; Kambhampati, P., The Temperature Dependence of the Photoluminescence of $CsPbBr_3$ Nanocrystals Reveals Phase Transitions and Homogeneous Linewidths. *J. Phys. Chem. C* **2021,** *125* (49), 27504-27508.

53. Pfingsten, O.; Klein, J.; Protesescu, L.; Bodnarchuk, M. I.; Kovalenko, M. V.; Bacher, G., Phonon Interaction and Phase Transition in Single Formamidinium Lead Bromide Quantum Dots. *Nano Lett.* **2018,** *18* (7), 4440-4446.

54. Wright, A. D.; Verdi, C.; Milot, R. L.; Eperon, G. E.; Perez-Osorio, M. A.; Snaith, H. J.; Giustino, F.; Johnston, M. B.; Herz, L. M., Electron-Phonon Coupling in Hybrid Lead Halide Perovskites. *Nat. Commun.* **2016,** *7*.

55. Debnath, T.; Sarker, D.; Huang, H.; Han, Z. K.; Dey, A.; Polavarapu, L.; Levchenko, S. V.; Feldmann, J., Coherent Vibrational Dynamics Reveals Lattice Anharmonicity in Organic-Inorganic Halide Perovskite Nanocrystals. *Nat. Commun.* **2021,** *12* (1), 2629.

56. Ghosh, S.; Shi, Q.; Pradhan, B.; Kumar, P.; Wang, Z.; Acharya, S.; Pal, S. K.; Pullerits, T.; Karki, K. J., Phonon Coupling with Excitons and Free Carriers in Formamidinium Lead Bromide Perovskite Nanocrystals. *J. Phys. Chem. Lett.* **2018,** *9* (15), 4245-4250.

57. Fu, M.; Tamarat, P.; Trebbia, J. B.; Bodnarchuk, M. I.; Kovalenko, M. V.; Even, J.; Lounis, B., Unraveling Exciton-Phonon Coupling in Individual $FAPbI_3$ Nanocrystals Emitting Near-Infrared Single Photons. *Nat. Commun.* **2018,** *9* (1), 3318.

58. Masada, S.; Yamada, T.; Tahara, H.; Hirori, H.; Saruyama, M.; Kawawaki, T.; Sato, R.; Teranishi, T.; Kanemitsu, Y., Effect of A-Site Cation on Photoluminescence Spectra of Single Lead Bromide Perovskite Nanocrystals. *Nano Lett.* **2020,** *20* (5), 4022-4028.

59. Tan, Z. K.; Moghaddam, R. S.; Lai, M. L.; Docampo, P.; Higler, R.; Deschler, F.; Price, M.; Sadhanala, A.; Pazos, L. M.; Credgington, D.; Hanusch, F.; Bein, T.; Snaith, H. J.; Friend, R. H., Bright Light-Emitting Diodes Based on Organometal Halide Perovskite. *Nat. Nanotechnol.* **2014,** *9* (9), 687-692.

60. Chiba, T.; Hayashi, Y.; Ebe, H.; Hoshi, K.; Sato, J.; Sato, S.; Pu, Y. J.; Ohisa, S.; Kido, J., Anion-Exchange Red Perovskite Quantum Dots with Ammonium Iodine Salts for Highly Efficient Light-Emitting Devices. *Nat. Photonics* **2018,** *12* (11), 681-687.

61. Lin, K.; Xing, J.; Quan, L. N.; de Arquer, F. P. G.; Gong, X.; Lu, J.; Xie, L.; Zhao, W.; Zhang, D.; Yan, C.; Li, W.; Liu, X.; Lu, Y.; Kirman, J.; Sargent, E. H.; Xiong, Q.; Wei, Z., Perovskite Light-Emitting Diodes with External Quantum Efficiency Exceeding 20 Per cent. *Nature* **2018,** *562* (7726), 245-248.

62. Burschka, J.; Pellet, N.; Moon, S. J.; Humphry-Baker, R.; Gao, P.; Nazeeruddin, M. K.; Gratzel, M., Sequential deposition as a route to high-performance perovskite-sensitized solar cells. *Nature* **2013,** *499* (7458), 316-319.

63. Jena, A. K.; Kulkarni, A.; Miyasaka, T., Halide Perovskite Photovoltaics: Background, Status, and Future Prospects. *Chem. Rev.* **2019,** *119* (5), 3036-3103.

64. Stranks, S. D.; Eperon, G. E.; Grancini, G.; Menelaou, C.; Alcocer, M. J.; Leijtens, T.; Herz, L. M.; Petrozza, A.; Snaith, H. J., Electron-Hole Diffusion Lengths Exceeding 1 Micrometer in an Organometal Trihalide Perovskite Absorber. *Science* **2013,** *342* (6156), 341-344.

65. Yin, W. J.; Shi, T. T.; Yan, Y. F., Unusual Defect Physics in $CH_3NH_3PbI_3$ Perovskite Solar Cell Absorber. *Appl. Phys. Lett.* **2014,** *104* (6).

66. Kang, J.; Wang, L. W., High Defect Tolerance in Lead Halide Perovskite $CsPbBr_3$. *J. Phys. Chem. Lett.* **2017,** *8* (2), 489-493.

67. Nedelcu, G.; Protesescu, L.; Yakunin, S.; Bodnarchuk, M. I.; Grotevent, M. J.; Kovalenko, M. V., Fast Anion-Exchange in Highly Luminescent Nanocrystals of Cesium Lead Halide Perovskites ($CsPbX_3$, X = Cl, Br, I). *Nano Lett.* **2015,** *15* (8), 5635-5640.

68. Parobek, D.; Dong, Y.; Qiao, T.; Rossi, D.; Son, D. H., Photoinduced Anion Exchange in Cesium Lead Halide Perovskite Nanocrystals. *J. Am. Chem. Soc.* **2017,** *139* (12), 4358-4361.

69. Artemyev, M. V.; Bibik, A. I.; Gurinovich, L. I.; Gaponenko, S. V.; Woggon, U., Evolution from Individual to Collective Electron States in a Dense Quantum Dot Ensemble. *Phys. Rev. B* **1999,** *60* (3), 1504-1506.

70. Tang, X. T.; Rossi, D.; Cheon, J.; Son, D. H., Effects of Electronic Coupling on Bright and Dark Excitons in a 2D Array of Strongly Confined $CsPbBr_3$ Quantum Dots. *Chem. Mater.* **2022,** *34* (16), 7181-7189.

71. Koole, R.; Liljeroth, P.; de Mello Donega, C.; Vanmaekelbergh, D.; Meijerink, A., Electronic Coupling and Exciton Energy Transfer in CdTe Quantum-Dot Molecules. *J. Am. Chem. Soc.* **2006,** *128* (32), 10436-10441.

72. Bol, A. A.; Meijerink, A., Long-Lived Mn^{2+} Emission in Nanocrystalline ZnS : Mn^{2+}. *Phys. Rev. B* **1998,** *58* (24), 15997-16000.

73. Beaulac, R.; Archer, P. I.; Ochsenbein, S. T.; Gamelin, D. R., Mn^{2+}-Doped CdSe Quantum Dots: New Inorganic Materials for Spin-Electronics and Spin-Photonics. *Adv. Funct. Mater.* **2008,** *18* (24), 3873-3891.

74. Chen, H. Y.; Chen, T. Y.; Berdugo, E.; Park, Y.; Lovering, K.; Son, D. H., Hot Electrons from Consecutive Exciton-Mn Energy Transfer in Mn-Doped Semiconductor Nanocrystals. *J. Phys. Chem. C* **2011,** *115* (23), 11407-11412.

75. Parobek, D.; Roman, B. J.; Dong, Y.; Jin, H.; Lee, E.; Sheldon, M.; Son, D. H., Exciton-to-Dopant Energy Transfer in Mn-Doped Cesium Lead Halide Perovskite Nanocrystals. *Nano Lett.* **2016,** *16* (12), 7376-7380.

76. Dong, Y.; Qiao, T.; Kim, D.; Rossi, D.; Ahn, S. J.; Son, D. H., Controlling Anisotropy of Quantum-Confined $CsPbBr_3$ Nanocrystals by Combined Use of Equilibrium and Kinetic Anisotropy. *Chem. Mater.* **2019,** *31* (15), 5655-5662.

77. Makarov, N. S.; Guo, S.; Isaienko, O.; Liu, W.; Robel, I.; Klimov, V. I., Spectral and Dynamical Properties of Single Excitons, Biexcitons, and Trions in Cesium-Lead-Halide Perovskite Quantum Dots. *Nano Lett.* **2016,** *16* (4), 2349-2362.

78. Li, Y.; Luo, X.; Ding, T.; Lu, X.; Wu, K., Size- and Halide-Dependent Auger Recombination in Lead Halide Perovskite Nanocrystals. *Angew. Chem. Int. Ed.* **2020,** *59* (34), 14292-14295.

79. Neukirch, A. J.; Nie, W.; Blancon, J. C.; Appavoo, K.; Tsai, H.; Sfeir, M. Y.; Katan, C.; Pedesseau, L.; Even, J.; Crochet, J. J.; Gupta, G.; Mohite, A. D.; Tretiak, S., Polaron Stabilization by Cooperative Lattice Distortion and Cation Rotations in Hybrid Perovskite Materials. *Nano Lett.* **2016,** *16* (6), 3809-3816.

80. Bonn, M.; Miyata, K.; Hendry, E.; Zhu, X. Y., Role of Dielectric Drag in Polaron Mobility in Lead Halide Perovskites. *ACS Energy Lett.* **2017,** *2* (11), 2555-2562.

81. Zhu, H.; Miyata, K.; Fu, Y.; Wang, J.; Joshi, P. P.; Niesner, D.; Williams, K. W.; Jin, S.; Zhu, X. Y., Screening in Crystalline Liquids Protects Energetic Carriers in Hybrid Perovskites. *Science* **2016,** *353* (6306), 1409-1413.

82. Frost, J. M.; Walsh, A., What Is Moving in Hybrid Halide Perovskite Solar Cells? *Acc. Chem. Res.* **2016,** *49* (3), 528-535.

83. Zhu, X. Y.; Podzorov, V., Charge Carriers in Hybrid Organic-Inorganic Lead Halide Perovskites Might Be Protected as Large Polarons. *J. Phys. Chem. Lett.* **2015,** *6* (23), 4758-4761.

84. Levchuk, I.; Osvet, A.; Tang, X.; Brandl, M.; Perea, J. D.; Hoegl, F.; Matt, G. J.; Hock, R.; Batentschuk, M.; Brabec, C. J., Brightly Luminescent and Color-Tunable

Formamidinium Lead Halide Perovskite $FAPbX_3$ (X = Cl, Br, I) Colloidal Nanocrystals. *Nano Lett.* **2017,** *17* (5), 2765-2770.

85. Brivio, F.; Walker, A. B.; Walsh, A., Structural and Electronic Properties of Hybrid Perovskites for High-Efficiency Thin-Film Photovoltaics from First-Principles. *APL Materials* **2013,** *1* (4).

86. Galkowski, K.; Mitioglu, A.; Miyata, A.; Plochocka, P.; Portugall, O.; Eperon, G. E.; Wang, J. T. W.; Stergiopoulos, T.; Stranks, S. D.; Snaith, H. J.; Nicholas, R. J., Determination of the Exciton Binding Energy and Effective Masses for Methylammonium and Formamidinium Lead Tri-Halide Perovskite Semiconductors. *Energy Environ. Sci.* **2016,** *9* (3), 962-970.

87. Baker, H.; Strandell, D.; Kambhampati, P., Emitting State of Bulk $CsPbBr_3$ Perovskite Nanocrystals Reveals a Quantum-Confined Excitonic Structure. *J. Phys. Chem. C* **2020,** *124* (34), 18816-18822.

88. Manser, J. S.; Christians, J. A.; Kamat, P. V., Intriguing Optoelectronic Properties of Metal Halide Perovskites. *Chem. Rev.* **2016,** *116* (21), 12956-13008.

89. Jing, P. T.; Zheng, J. J.; Ikezawa, M.; Liu, X. Y.; Lv, S. Z.; Kong, X. G.; Zhao, J. L.; Masumoto, Y., Temperature-Dependent Photoluminescence of CdSe-Core CdS/CdZnS/ZnS-Multishell Quantum Dots. *J. Phys. Chem. C* **2009,** *113* (31), 13545-13550.

90. Gramlich, M.; Swift, M. W.; Lampe, C.; Lyons, J. L.; Doblinger, M.; Efros, A. L.; Sercel, P. C.; Urban, A. S., Dark and Bright Excitons in Halide Perovskite Nanoplatelets. *Adv. Sci.* **2022,** *9* (5), e2103013.

91. Kagan, C. R.; Lifshitz, E.; Sargent, E. H.; Talapin, D. V., Building Devices from Colloidal Quantum Dots. *Science* **2016,** *353* (6302), aac5523.

92. Kagan, C. R.; Murray, C. B., Charge Transport in Strongly Coupled Quantum Dot Solids. *Nat. Nanotechnol.* **2015,** *10* (12), 1013-1026.

93. Artemyev, M. V.; Woggon, U.; Jaschinski, H.; Gurinovich, L. I.; Gaponenko, S. V., Spectroscopic Study of Electronic States in an Ensemble of Close-Packed CdSe Nanocrystals. *J. Phys. Chem. B* **2000,** *104* (49), 11617-11621.

94. Williams, K. J.; Tisdale, W. A.; Leschkies, K. S.; Haugstad, G.; Norris, D. J.; Aydil, E. S.; Zhu, X. Y., Strong Electronic Coupling in Two-Dimensional Assemblies of Colloidal PbSe Quantum Sots. *ACS Nano* **2009,** *3* (6), 1532-1538.

95. Law, M.; Luther, J. M.; Song, Q.; Hughes, B. K.; Perkins, C. L.; Nozik, A. J., Structural, Optical, and Electrical Properties of PbSe Nanocrystal Solids Treated Thermally or with Simple Amines. *J. Am. Chem. Soc.* **2008,** *130* (18), 5974-5985.

96. Thuy, U. T. D.; Thuy, P. T.; Liem, N. Q.; Li, L.; Reiss, P., Comparative photoluminescence study of close-packed and colloidal InP/ZnS quantum dots. *Appl. Phys. Lett.* **2010,** *96* (7).

97. Talapin, D. V.; Murray, C. B., PbSe Nanocrystal Solids for n- and p-Channel Thin Film Field-Effect Transistors. *Science* **2005,** *310* (5745), 86-89.

98. Yu, D.; Wang, C.; Guyot-Sionnest, P., n-Type Conducting CdSe Nanocrystal Solids. *Science* **2003,** *300* (5623), 1277-1280.

99. Lee, J. S.; Kovalenko, M. V.; Huang, J.; Chung, D. S.; Talapin, D. V., Band-Like Transport, High Electron Mobility and High Photoconductivity in All-Inorganic Nanocrystal Arrays. *Nat. Nanotechnol.* **2011,** *6* (6), 348-352.

100. Liu, Y.; Tolentino, J.; Gibbs, M.; Ihly, R.; Perkins, C. L.; Liu, Y.; Crawford, N.; Hemminger, J. C.; Law, M., PbSe Quantum Dot Field-Effect Transistors with Air-Stable Electron Mobilities Above 7 cm^2 V^{-1} s^{-1}. *Nano Lett.* **2013,** *13* (4), 1578-1587.

101. Lan, X.; Chen, M.; Hudson, M. H.; Kamysbayev, V.; Wang, Y.; Guyot-Sionnest, P.; Talapin, D. V., Quantum Dot Solids Showing State-Resolved Band-Like Transport. *Nat. Mater.* **2020,** *19* (3), 323-329.

102. Crisp, R. W.; Schrauben, J. N.; Beard, M. C.; Luther, J. M.; Johnson, J. C., Coherent Exciton Delocalization in Strongly Coupled Quantum Dot Arrays. *Nano Lett.* **2013,** *13* (10), 4862-4869.

103. Cui, J.; Panfil, Y. E.; Koley, S.; Shamalia, D.; Waiskopf, N.; Remennik, S.; Popov, I.; Oded, M.; Banin, U., Colloidal Quantum Dot Molecules Manifesting Quantum Coupling at Room Temperature. *Nat. Commun.* **2019,** *10* (1), 5401.

104. Panfil, Y. E.; Shamalia, D.; Cui, J.; Koley, S.; Banin, U., Electronic Coupling in Colloidal Quantum Dot Molecules; the Case of CdSe/CdS Core/Shell Homodimers. *J. Chem. Phys.* **2019,** *151* (22), 224501.

105. Fan, J. Z.; Vafaie, M.; Bertens, K.; Sytnyk, M.; Pina, J. M.; Sagar, L. K.; Ouellette, O.; Proppe, A. H.; Rasouli, A. S.; Gao, Y.; Baek, S. W.; Chen, B.; Laquai, F.; Hoogland, S.; Arquer, F. P. G.; Heiss, W.; Sargent, E. H., Micron Thick Colloidal Quantum Dot Solids. *Nano Lett.* **2020,** *20* (7), 5284-5291.

106. Tong, Y.; Yao, E. P.; Manzi, A.; Bladt, E.; Wang, K.; Doblinger, M.; Bals, S.; Muller-Buschbaum, P.; Urban, A. S.; Polavarapu, L.; Feldmann, J., Spontaneous Self-Assembly of Perovskite Nanocrystals into Electronically Coupled Supercrystals: Toward Filling the Green Gap. *Adv. Mater. (Weinheim, Ger.)* **2018**, e1801117.

107. van der Burgt, J. S.; Geuchies, J. J.; van der Meer, B.; Vanrompay, H.; Zanaga, D.; Zhang, Y.; Albrecht, W.; Petukhov, A. V.; Filion, L.; Bals, S.; Swart, I.; Vanmaekelbergh, D., Cuboidal Supraparticles Self-Assembled from Cubic $CsPbBr_3$ Perovskite Nanocrystals. *J. Phys. Chem. C* **2018,** *122* (27), 15706-15712.

108. Imran, M.; Ijaz, P.; Baranov, D.; Goldoni, L.; Petralanda, U.; Akkerman, Q.; Abdelhady, A. L.; Prato, M.; Bianchini, P.; Infante, I.; Manna, L., Shape-Pure, Nearly Monodispersed $CsPbBr_3$ Nanocubes Prepared Using Secondary Aliphatic Amines. *Nano Lett.* **2018,** *18* (12), 7822-7831.

109. Raino, G.; Becker, M. A.; Bodnarchuk, M. I.; Mahrt, R. F.; Kovalenko, M. V.; Stoferle, T., Superfluorescence from lead halide perovskite quantum dot superlattices. *Nature* **2018,** *563* (7733), 671-675.

110. Baranov, D.; Toso, S.; Imran, M.; Manna, L., Investigation into the Photoluminescence Red Shift in Cesium Lead Bromide Nanocrystal Superlattices. *J. Phys. Chem. Lett.* **2019,** *10* (3), 655-660.

111. Rainò, G.; Becker, M. A.; Bodnarchuk, M. I.; Mahrt, R. F.; Kovalenko, M. V.; Stöferle, T., Superfluorescence from Lead Halide Perovskite Quantum Dot Superlattices. *Nature* **2018,** *563* (7733), 671-675.

112. Harris, R. D.; Bettis Homan, S.; Kodaimati, M.; He, C.; Nepomnyashchii, A. B.; Swenson, N. K.; Lian, S.; Calzada, R.; Weiss, E. A., Electronic Processes within Quantum Dot-Molecule Complexes. *Chem. Rev.* **2016,** *116* (21), 12865-12919.

113. Yang, J.; Wise, F. W., Effects of Disorder on Electronic Properties of Nanocrystal Assemblies. *J. Phys. Chem. C* **2015,** *119* (6), 3338-3347.

114. Puthenpurayil, J.; Cheng, O. H.; Qiao, T.; Rossi, D.; Son, D. H., On the Determination of Absorption Cross Section of Colloidal Lead Halide Perovskite Quantum Dots. *J. Chem. Phys.* **2019,** *151* (15), 154706.

115. Rossi, D.; Wang, H.; Dong, Y.; Qiao, T.; Qian, X.; Son, D. H., Light-Induced Activation of Forbidden Exciton Transition in Strongly Confined Perovskite Quantum Dots. *ACS Nano* **2018,** *12* (12), 12436-12443.

116. Kagan, C. R.; Murray, C. B.; Bawendi, M. G., Long-Range Resonance Transfer of Electronic Excitations in Close-Packed CdSe Quantum-Dot Solids. *Phys. Rev. B: Condens. Matter* **1996,** *54* (12), 8633-8643.

117. Crooker, S. A.; Hollingsworth, J. A.; Tretiak, S.; Klimov, V. I., Spectrally Resolved Dynamics of Energy Transfer in Quantum-Dot Assemblies: Towards Engineered Energy Flows in Artificial Materials. *Phys. Rev. Lett.* **2002,** *89* (18), 186802.

118. Hudait, B.; Dutta, S. K.; Patra, A.; Nasipuri, D.; Pradhan, N., Facets Directed Connecting Perovskite Nanocrystals. *J. Am. Chem. Soc.* **2020,** *142* (15), 7207-7217.

119. Nagaoka, Y.; Hills-Kimball, K.; Tan, R.; Li, R.; Wang, Z.; Chen, O., Nanocube Superlattices of Cesium Lead Bromide Perovskites and Pressure-Induced Phase

Transformations at Atomic and Mesoscale Levels. *Adv. Mater. (Weinheim, Ger.)* **2017,** *29* (18).

120. Iaru, C. M.; Geuchies, J. J.; Koenraad, P. M.; Vanmaekelbergh, D.; Silov, A. Y., Strong Carrier-Phonon Coupling in Lead Halide Perovskite Nanocrystals. *ACS Nano* **2017,** *11* (11), 11024-11030.

121. Potma, E. O.; Wiersma, D. A., Exciton Superradiance in Aggregates: The Effect of Disorder, Higher Order Exciton-Phonon Coupling and Dimensionality. *J. Chem. Phys.* **1998,** *108* (12), 4894-4903.

122. Wubs, M.; Knoester, J., Exchange Narrowing in Dynamically Disordered Molecular Aggregates. *Chem. Phys. Lett.* **1998,** *284* (1-2), 63-70.

123. Rodina, A.; Efros, A. L., Magnetic Properties of Nonmagnetic Nanostructures: Dangling Bond Magnetic Polaron in CdSe Nanocrystals. *Nano Lett.* **2015,** *15* (6), 4214-4222.

124. Rodina, A. V.; Efros, A. L., Radiative Recombination from Dark Excitons in Nanocrystals: Activation Mechanisms and Polarization Properties. *Phys. Rev. B* **2016,** *93* (15), 155427-155442.

125. Oron, D.; Aharoni, A.; de Mello Donega, C.; van Rijssel, J.; Meijerink, A.; Banin, U., Universal Role of Discrete Acoustic Phonons in the Low-Temperature Optical Emission of Colloidal Quantum Dots. *Phys. Rev. Lett.* **2009,** *102* (17), 177402.

126. Toso, S.; Baranov, D.; Giannini, C.; Marras, S.; Manna, L., Wide-Angle X-ray Diffraction Evidence of Structural Coherence in $CsPbBr_3$ Nanocrystal Superlattices. *ACS Mater. Lett.* **2019,** *1* (2), 272-276.

127. Baranov, D.; Fieramosca, A.; Yang, R. X.; Polimeno, L.; Lerario, G.; Toso, S.; Giansante, C.; Giorgi, M.; Tan, L. Z.; Sanvitto, D.; Manna, L., Aging of Self-Assembled Lead Halide Perovskite Nanocrystal Superlattices: Effects on Photoluminescence and Energy Transfer. *ACS Nano* **2021,** *15* (1), 650-664.

128. Zhou, C.; Zhong, Y.; Dong, H.; Zheng, W.; Tan, J.; Jie, Q.; Pan, A.; Zhang, L.; Xie, W., Cooperative Excitonic Quantum Ensemble in Perovskite-Assembly Superlattice Microcavities. *Nat. Commun.* **2020,** *11* (1), 329.

129. Findik, G.; Biliroglu, M.; Seyitliyev, D.; Mendes, J.; Barrette, A.; Ardekani, H.; Lei, L.; Dong, Q.; So, F.; Gundogdu, K., High-Temperature Superfluorescence in Methyl Ammonium Lead Iodide. *Nat. Photonics* **2021,** *15* (9), 676-680.

130. Biliroglu, M.; Findik, G.; Mendes, J.; Seyitliyev, D.; Lei, L.; Dong, Q.; Mehta, Y.; Temnov, V. V.; So, F.; Gundogdu, K., Room-Temperature Superfluorescence in Hybrid Perovskites and its Origins. *Nat. Photonics* **2022,** *16* (4), 324-329.

131. Krieg, F.; Sercel, P. C.; Burian, M.; Andrusiv, H.; Bodnarchuk, M. I.; Stoferle, T.; Mahrt, R. F.; Naumenko, D.; Amenitsch, H.; Raino, G.; Kovalenko, M. V., Monodisperse Long-Chain Sulfobetaine-Capped $CsPbBr_3$ Nanocrystals and Their Superfluorescent Assemblies. *ACS Cent. Sci.* **2021,** *7* (1), 135-144.

132. Toso, S.; Baranov, D.; Altamura, D.; Scattarella, F.; Dahl, J.; Wang, X.; Marras, S.; Alivisatos, A. P.; Singer, A.; Giannini, C.; Manna, L., Multilayer Diffraction Reveals That Colloidal Superlattices Approach the Structural Perfection of Single Crystals. *ACS Nano* **2021,** *15* (4), 6243-6256.

133. Blach, D. D.; Lumsargis, V. A.; Clark, D. E.; Chuang, C.; Wang, K.; Dou, L.; Schaller, R. D.; Cao, J.; Li, C. W.; Huang, L., Superradiance and Exciton Delocalization in Perovskite Quantum Dot Superlattices. *Nano Lett.* **2022,** *22* (19), 7811-7818.

134. Boehme, S. C.; Bodnarchuk, M. I.; Burian, M.; Bertolotti, F.; Cherniukh, I.; Bernasconi, C.; Zhu, C.; Erni, R.; Amenitsch, H.; Naumenko, D.; Andrusiv, H.; Semkiv, N.; John, R. A.; Baldwin, A.; Galkowski, K.; Masciocchi, N.; Stranks, S. D.; Raino, G.; Guagliardi, A.; Kovalenko, M. V., Strongly Confined $CsPbBr_3$ Quantum Dots as Quantum Emitters and Building Blocks for Rhombic Superlattices. *ACS Nano* **2023**.